DEPARTMENT OF PHYSICS
UNIVERSITY OF JYVÄSKYLÄ
RESEARCH REPORT No. 2/2004

STUDIES OF STRUCTURES AND MELTING OF SMALL METAL CLUSTERS

BY
KIRSI MANNINEN

Academic Dissertation
for the Degree of
Doctor of Philosophy

Jyväskylä, Finland
July 2004

ISBN 978-951-39-3151-3

URN:ISBN:978-951-39-3151-3

DEPARTMENT OF PHYSICS
UNIVERSITY OF JYVÄSKYLÄ
RESEARCH REPORT No. 2/2004

STUDIES OF STRUCTURES AND MELTING OF SMALL METAL CLUSTERS

BY
KIRSI MANNINEN

Academic Dissertation
for the Degree of
Doctor of Philosophy

To be presented, by permission of the
Faculty of Mathematics and Natural Sciences
of the University of Jyväskylä,
for public examination in Auditorium FYS-1 of the
University of Jyväskylä on July 23, 2004
at 12 o'clock noon

Jyväskylä, Finland
July 2004

Preface

The work described in this dissertation was carried out by the author in the department of Physics at the University of Jyväskylä from September 2000 to July 2004.

I would like to thank my supervisor, Professor Matti Manninen, for his help, encouragement and inspiring guidance during the work. I am also grateful to Dr. Jaakko Akola for his collaboration and useful discussions. Dr. Anniina Rytkönen introduced me the basic methods of computational cluster physics, and I am deeply indebted to her for this introduction. I would also thank Dr. Hannu Häkkinen for co-operations and helping me with specific problems and answering my questions.

I am very grateful for Vera Hansper for her helpful suggestions and corrections in the manuscript. I also acknowledge useful discussions with Dr. Pekka Koskinen, Kari Rytkönen and Kimmo Kärkkäinen. A warm thank you for their friendship is extended to Heli Honkanen, Päivi Nieminen, Jussi Toivanen, and Matias Aunola, as well as all those whom I may have forgotten to mention. I would also like to thank the staff of the Department of Physics for providing an inspiring work atmosphere and for assistance with practical problems.

The financial support from the Väisälä foundation are gratefully acknowledged. The computational resources for this thesis were provided by the CSC - The Finnish IT Center for Science.

Finally, my warmest thanks to my loving spouse Jarno for his encouragement to do housework and of course thanks to my sons Henri, Ossi and Topi for giving me something to do. Of the many people who helped, I am particularly grateful to my mother-in-law, Terttu Manninen, for encouragement and for providing practical help with the children.

Jyväskylä, July 2004

Kirsi Manninen

Abstract

This thesis is a review of five publications, where small and medium-sized hard sphere and sodium clusters are studied. The first two publications focus on close-packed clusters and especially on their structure. Monte Carlo method and Metropolis algorithm were used to study structures of close-packed clusters with N = 1-110 hard spheres. Two types of contact interactions were used: pair-potential and tight-binding interactions. A new selection of magic numbers were found (N = 12, 26, 38, 50, 59, 61, 68, 75, 79, 86, 100, 102). The results were applied to Al_{100}. The density-functional calculations show that for aluminum the strain-free close-packed structures are lower in total energy than the corresponding icosahedral and decahedral isomers.

The three other publications present studies of sodium clusters. The initial motivation for these studies were to explain the unusual melting temperature variation. It became evident that in order to explain the experimental results it was necessary to use an *ab initio* molecular dynamic method instead of a semi-classical molecular dynamic simulations method.

The *ab initio* molecular dynamics method was used to simulate the melting of Na_{59}^{+} and Na_{93}^{+}. The results gave melting temperatures for Na_{59}^{+} and Na_{93}^{+} in agreement with the experimental results. The latent heat of fusion related to the melting of Na_{59}^{+} could be calculated, but in the case of Na_{93}^{+} it was too small to be determined. The electronic structure of sodium clusters is consistent with jellium model predictions. The electron density of states of Na_{55}^{+}, Na_{59}^{+} and Na_{93}^{+} were compared with the experimental photoelectron spectra and the agreement is excellent.

List of publications

This thesis consists of an introductory part and of the following publications:

I Stacking faults in close-packed clusters
K. Manninen, and M. Manninen
Eur. Phys. J. D. **20**, (2002) 243.

II Close-Packing of Clusters: Application to Al_{100}
K. Manninen, J. Akola, and M. Manninen
Phys. Rev. B **68** (2003) 235412.

III Influence of electronic and geometric properties on melting of sodium clusters
K. Manninen, A. Rytkönen, and M. Manninen
Eur. Phys. J. D. **29** (2004) 39.

IV The electronic structure and thermal behavior of a magic Na_{59}^{+} cluster
K. Manninen, H. Häkkinen, and M. Manninen
Phys. Rev. A. (accepted for publication).

V Ab initio simulation of Na_{59}^{+} and Na_{93}^{+}
K. Manninen, H. Häkkinen, and M. Manninen
Submitted for publications Computational Material Science.

The author of this thesis has written draft versions of all the papers expect for paper II, which was written in co-operation with Dr. Jaakko Akola. The author has performed all the numerical work expect for the electronic structure calculations for paper II. The author has participated in the interpretation of the results in all the papers.

Contents

1 Introduction **1**

2 The structure of clusters **3**
2.1 Background . . . 3
2.2 Types of structures . . . 3
2.2.1 Icosahedral structures . . . 4
2.2.2 FCC, HCP and other close-packed clusters . . . 5
2.3 Magic numbers . . . 6
2.3.1 Observation of magic numbers . . . 6
2.4 History of calculations . . . 8
2.4.1 Potentials and calculation methods . . . 8
2.4.2 Examples of earlier simulations . . . 9
2.5 Motivation to study close-packed clusters . . . 9
2.6 Monte Carlo and Metropolis algorithm . . . 10
2.7 Results . . . 12
2.7.1 Geometries of the hard sphere clusters . . . 12
2.7.2 Magic numbers of hard sphere clusters . . . 15
2.7.3 Moments of inertia . . . 17

3 Melting of sodium clusters **19**
3.1 Background . . . 19
3.2 Determining the melting temperature . . . 21
3.3 Earlier experiments and simulations . . . 22
3.4 Latent heat of fusion, width of phase transition and binding energy . . . 23
3.5 Electronic and geometric magic numbers . . . 24
3.6 Ionization potential . . . 24
3.7 Negative heat capacity . . . 25
3.8 One of experimental methods . . . 26
3.9 Theoretical methods . . . 26
3.9.1 Molecular dynamics simulation method . . . 27
3.9.2 Ab initio molecular dynamics . . . 29
3.10 Results . . . 33
3.10.1 Semi-classical simulations . . . 33
3.10.2 Ab initio simulations . . . 37

4 Electronic structure **45**
4.1 Background 45
4.2 Jellium model 47
4.3 Experimental observations 47
4.4 Results 48
4.4.1 Electronic structure calculations of Al_{100} isomers 52

5 Summary **55**

References **57**

1 Introduction

Clusters are finite aggregates of atoms or molecules that contain from a few to tens of thousands of atoms. The number of atoms or molecules are countable and they exhibit unique physical and chemical phenomena. The main issues in cluster science are the unique structures, stabilities, electronic spectra, and thermodynamical properties of clusters, and their size-dependent evolution. Small clusters often present significant physical and chemical differences with respect to the atoms or molecules and the bulk material, because the size of the clusters lies somewhere in between an ensemble of single atoms or molecules and a bulk solid material. This is why clusters provide a bridge between the size of the atoms and bulk material. The evolution of the properties from atoms to bulk material is very interesting and gives the possibility for new technological applications like nanoelectronics. One aim in material science is to obtain smaller and smaller devices with precise properties.

The science of clusters has expanded rapidly in the last twenty-five years and at the same time new experimental techniques have become available and computational power has increased. The discovery of molecular beams produced by free-jet expansion was very important, because it made it possible to produce mass-selected clusters. After this discovery the amount of experimental research of clusters increased dramatically.

Structure has a central role in cluster science and it has an influence to many properties of clusters. Much experimental and theoretical effort has been expended in order to characterize the structure of clusters. Even though small clusters may form close-packed face-centered-cubic (FCC) or hexagonal closed-packed (HCP) structures like the bulk, clusters may prefer icosahedral or decahedral structures, depending on their size. The size dependence of the different properties is indeed one of the unique phenomena for clusters. Due to the fact that the proportion of the surface atoms in a cluster scales with cluster radius R as 1/R, one should expect that the melting behavior as well as other properties are monotonic, smooth functions of the cluster size. However, there is evidence indicating, that for example, the ionization potential does not evolve gradually as the cluster size is increased, but exhibits an irregular dependence on cluster size. According to experiments and simulations melting temperature is also not a monotonically increasing function of cluster size for the small sodium clusters. Some properties even depend on whether a cluster contains an even or odd number of electrons.

Over the years a lot of work has been devoted to alkali-metal clusters and in particular to sodium clusters. The reason for this is that sodium clusters can be generated easily in conventional sources under supersonic adiabatic expansion conditions. Of course, new experimental results also lead to an increase in theoretical study.

This thesis progresses in the following way. In Chapter 2, I attempt to provide a new selection of geometrically magic cluster sizes for close-packed clusters. In addition, one example is provided to illustrate the justification of the used method. In Chapter 3, I first present a brief introduction to the basic concepts and past work relevant to the melting transition in clusters. After that I explain the methods used in studying the melting transition and provide conclusions including also the results of *ab initio* simulations made in our department before my thesis work.

In Chapter 4, I discuss the electronic structure of sodium clusters on the basis of the same simulations made for the melting transition. The time-evolution of the Kohn-Sham states during the heating simulations is also discussed. Finally, in the conclusion, I summarize the achievements of the work described in this thesis, and suggest some possible future directions. Comprehensive introductions into each area are given at the beginning of each chapter.

2 The structure of clusters

2.1 Background

Stabilities, ionization potentials, electronic properties [1], vibrational spectra, polarizabilities [2], electrical transport properties [3] and the thermal properties [4] of clusters depend on the structures of clusters. Because so many interesting properties largely largely on the cluster structure, a complete description of the relevant isomer configurations for each cluster size is highly desirable.

There are many different isomers, especially at the larger cluster sizes, because the number of different isomers increases exponentially with cluster size. The total number of isomers becomes astronomically large as N increases [5]. Therefore, studies of properties of atomic clusters are difficult even for the case of relatively few atoms. For example at $N = 13$ there are already at least 988 minima [6]. This is why the *ab initio* calculations of atomic clusters are very time-consuming.

In bulk crystals the structure is characterized by the periodicity of a lattice, whereas in clusters the periodicity is not required. Large clusters have a small portion of surface atoms and so the surface energy has a negligible effect on their bulk-like atomic structure. But when the cluster size decreases the surface energy becomes more important and it might, and does, change the atomic structure of the cluster to one with lower surface energy.

2.2 Types of structures

The atomic clusters can adopt several different kinds of structures. The three main types of ordered structures are decahedral, icosahedral and crystal structures such as FCC, HCP and body-centered cubic (BCC) structures. The decahedral structures are based on pentagonal bipyramids and have a single fivefold axis of symmetry, whereas the icosahedral structures have six fivefold axes of symmetry.

It is usually found that, at small sizes, icosahedra prevail. On the other hand, decahedra are usually found at intermediate sizes and crystalline structures in the limit of large N. The crossover sizes from icosahedra to decahedra and from decahedra to

crystalline structures strongly depend on the system under study.

2.2.1 Icosahedral structures

Experimentally and theoretically many clusters are found to have fivefold axes of symmetry even if this structure is forbidden for the symmetry of the standard lattices. It has been know over 40 years that many of the lowest energy structures were based on Mackey icosahedra [7], especially in the case of rare gases (neon, argon, and krypton). The icosahedral growth sequence has been shown experimentally from the intensity variations in the mass spectra [8, 9] and from the electron diffraction [10, 11] for sizes of up to at least 750 atoms.

Echt *et al.* [12] found the first experimental evidence of the existence of magic numbers ($N = 13$, 55, 147) corresponding to icosahedral shells for clusters. Icosahedral structures were soon found also from other elements (argon [9], sodium [13, 14], potassium, cobalt [15, 16], barium [17], magnesium [18], calcium [19], nickel [16]) and molecular clusters [20].

The lowest energy structures are not necessarily icosahedral in the sizes between the complete icosahedron. If the shell of a cluster is not filled, it is free to deform to minimize the energy leading to different structures such as decahedral [I, 21, 22, 23] or cubic. For example an 38-atom truncated octahedron is observed experimentally in small gold clusters using extended x-ray absorption fine structure spectra [24]. It is also seen experimentally in ligated 38-atom platinum clusters [25].

Icosahedral packing is found only in relatively small clusters, which have a high surface-to-volume ratio. This is because icosahedral symmetry optimizes the surface energy at the expense of large internal strain. So, if the clusters are relatively small and have high surface-to-volume ratio, the icosahedral structure is energetically the best structure, but when the size of the cluster is increased and the surface-to-volume ratio becomes smaller, the internal strain is so big that icosahedral symmetry is no longer the best structure energetically.

The smallest icosahedra are presented in Fig. 2.1. Icosahedra are made up of 20 identical tetrahedra possessing a common vertex and connected with each other through adjacent faces, each of which forms twinning planes. A common rule is that if an icosahedron has n complete layers, it possesses $n + 1$ atoms on each edge just as the constituting tetrahedra. The smallest icosahedron is the 13-atom icosahedron with two atoms on each edge. The 13-atom icosahedron is an extremely common structure for rare gases [12], molecular clusters [26] and also exists in metals [27].

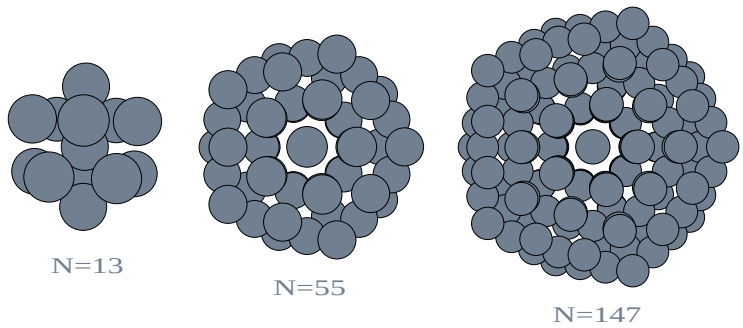

Figure 2.1: Smallest icosahedral structures.

2.2.2 FCC, HCP and other close-packed clusters

The FCC is the thermodynamically preferred structure in larger cluster sizes ($N > 1000$) [28]. The best structures of nickel are icosahedra at sizes $N < 1700$. At sizes $1700 < N < 2300$ decahedra prevail and for $N > 2300$ FCC polyhedra[29]. Lee and Stein [11] showed that the structure of argon clusters is icosahedral for up to 1500 atoms and then undergoes a smooth transition to FCC over the range of 1500 to 3500 atoms.

Close-packed structures can consist of different kind of packing of (111) layers. The pure HCP-structure have an arrangement ABABAB.., where the letters represent the different types of layers. When the structure is pure FCC, the arrangement is ABCABC... Of course these layers can be arranged in many different ways. Structures with internal stacking faults (layer which cause the defect inside the cluster) are also possible. Using the (111) layers we can form, for example, tetrahedra, octahedra and their truncated forms, which have triangular, square and hexagonal faces [27]. The Wulff structure can also be formed. The Wulff structure is the structure that possesses the lowest surface energy for a fixed volume and hence represents the ideal structure that the crystal would take.

The bulk FCC and HCP lattices have twelve nearest neighbours per atom. The surface energy depends on the coordination number of the surface atoms. It is nine for the close-packed (111) surface, and eight for (100) surface and seven for (110) surface. The optimal shape of close-packed clusters results from the balance between maximizing the proportion of (111) facets and minimizing the fraction of atoms in the surface layer. The tetrahedron and octahedron are FCC structures that have only 111 facets but they are not very spherical. The optimal FCC structure is the truncated octahedron with regular hexagonal faces. The structure approximates more and more the Wulff polyhedron [29] after further faceting.

2.3 Magic numbers

The stability of small clusters can strongly depend on the size. Clusters with a certain number of atoms can be significantly more stable (magic) than clusters with one atom more or one atom less [12]. Such stable clusters are caused by either the electronic or geometric closed shells. The electronically magic clusters have the total number of valence electrons in the clusters exactly right to completely fill an electronic shell. On the other hand, the geometrically magic clusters have the exact number of atoms to fill up, for example, icosahedral shell. Cluster sizes of particular stability are often revealed experimentally in a mass spectrum by discontinuous breaks or maxima in the envelope of peak intensities [15]. Similarly, alkali metal clusters show magic numbers corresponding to filled electronic shells of a jellium-like system [13, 30].

For small clusters, the magic numbers based on icosahedral geometry are dominant [7]. The so called geometric magic numbers corresponding to the complete icosahedron can be calculated from the formula $N = (10n^3 - 15n^2 + 11n - 3)/3$, for $n = 2,3,..$ leading to 13, 55, 147, 309,.. Icosahedral packing is common to many metals (e.g. Na, Mg, Cu) and rare gases and which is easily verified experimentally from the magic numbers [27, 31].

The geometrical magic numbers $N = 13$ and $N = 38$ are very special since they have been seen in nearly every magic number series. Exceptions also exist: Zinc and cadmium clusters interacting with a Gupta potential [32] do not have minima at $N = 13$ and at $N = 38$, but instead at $N = 55$. The cubic cluster size $N = 38$ has been found in many studies [I, 22, 33, 34]. The icosahedral cluster $N = 55$, which is also a magic number in many studies is, however, not as special size as $N = 13$ and $N = 38$ are: There are more than one study which show this [35].

2.3.1 Observation of magic numbers

Echt *et al.* [12] found the first experimental evidence of the existence of magic cluster sizes for free xenon clusters. The most prominent intensity peaks occur at $N = 13$, 19, 25, 55, 71, 87 and 147. Cluster sizes of $N = 23$, 81, 101 and 135 also show intensity peaks, but smaller than the first ones. Rare gas cluster ions except for He show magic numbers that can be interpreted in terms of filled geometrical shells and subshells of Mackay icosahedra [10, 36].

Branz *et al.* studied both neutral and charged $(C_{60})_N$ clusters using mass spectra. They found that at 490 K particularly stable clusters are $N = 13$, 19, 39, 46, 49, 55, 116, 131, 147, which indicated the presence of icosahedral structures. A different set of stable clusters was found at $N = 38$, 48, 58, 68, 71, 75, 77, 84, 98 at a temperature

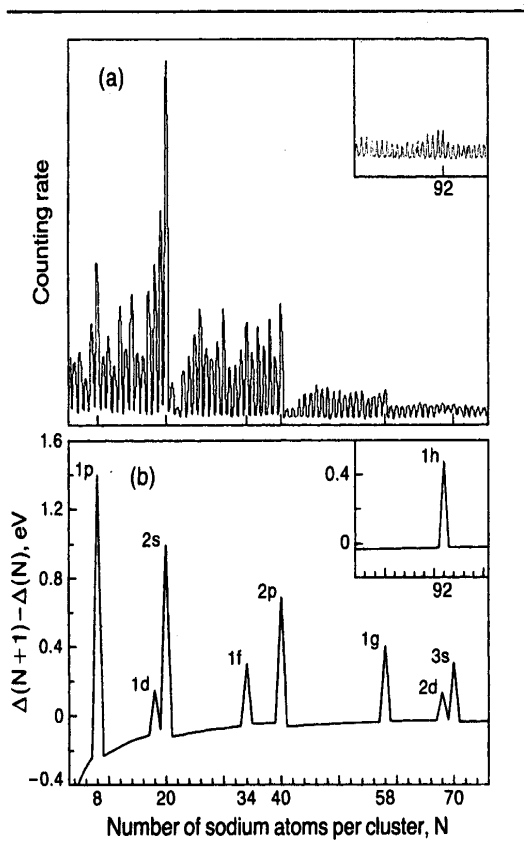

Figure 2.2: a) The experimental mass spectrum of sodium clusters and b) the calculated change in the electronic energy difference as a function of cluster size according to ref. [13]. The labels of the peaks corresponds to the close-shell orbitals.

near 585 K. According to Branz *et al.* this set of stable clusters correlates rather well with close-packed and decahedral structures [37]. Simple metal clusters show magic numbers originating from the electronic shell structure. Knight *et al.* [13] discovered the shell structure and magic numbers from the experimental abundance spectra of sodium clusters (shown in Fig. 2.2).

Different potentials give different magic numbers. Doye and Wales found magic numbers at $N = 13, 19, 23, 26, 29, 32, 34, 38, 42, 46, 57, 76, 94$ using a modified Dzugutov potential [33]. The putative Dzugutov potential gives magic numbers at $N = 13, 19, 23, 29, 33, 38, 42, 46, 52, 57, 60, 66, 86, 100$ [38]. The Pacheco and Prates-Ramalho potential gives the energy minimas at $N = 13, 31, 33, 35, 38, 48, 50, 59$. Doye *et al.* pointed out that minima are based on icosahedral packing for up to $N = 15$, but above this size the lowest energy structures are decahedral or close-packed. For comparison they used the spherically averaged Girifalco potential, which yields minimas at $N = 13, 26, 29, 31, 33, 35, 38, 50, 57, 59$ [34]. On the other hand, polytetrahedral

clusters studied by the modified Dzugutov potential have magic numbers at $N = 13$, 19, 23, 26, 29, 38, 57, 76, 94, 111, 129, 146 [35].

2.4 History of calculations

2.4.1 Potentials and calculation methods

Several different potentials have been used to study the structures of clusters. The most studied is the Lennard-Jones (LJ) potential, which is conventionally written as

$$V_{LJ}(r) = 4\epsilon \left[\left(\frac{\sigma}{r_{ij}} \right)^{-12} - \left(\frac{\sigma}{r_{ij}} \right)^{-6} \right], \tag{2.1}$$

where ϵ characterizes the well depth of the pair interaction and σ is the hard sphere radius of the atom. This potential gives a good description of the interaction in Van der Waals clusters such as those formed by the noble gases.

The covalently bonded molecules are widely modeled using the Morse potential [39, 40]. LJ and Morse potentials describe the interactions between atoms with no relation to the electrons in the system. In the case of metals the problem arises from the fact that the valence electrons are delocalised over a large number of atoms and so the bonding between two atoms is highly dependent on the local environment. Consequently LJ and Morse potentials do not give an accurate description of the interactions for metallic systems. This has led to the development of potentials for different kinds of metals. For example, the Dzugutov potential [38], modified Dzugutov potential [33] and the potential of Pacheco and Prates-Ramalho [34] have been used. Another possibility is to use many-atom potentials of tight-binding or embedded atom methods.

Many techniques have been developed for searching the ground state geometry. Simulated annealing techniques based on either Monte Carlo or molecular dynamics methods model the quenching of a cluster from a random high temperature geometry into a low energy geometry. Also *ab initio* methods (like Born-Oppenheimer local-spin-density molecular-dynamics (BO-LSD-MD) and Car-Parrinello methods) are used for systematic study of small cluster geometries. Usually the cluster sizes studied with *ab initio* methods are small ($N \leq 20$) [41, 42, 43].

2.4.2 Examples of earlier simulations

Northby [8] has systematically studied the size range $13 < N < 147$ using the LJ potential to find the lowest energy minima based on icosahedral structures. Some of his results have since been confirmed theoretically by others [21, 22, 44, 45]. Doye, Miller and Wales [23] have also used the LJ potential to characterize the potential energy surfaces of clusters containing 13, 19, 31, 38, 55 and 75 atoms [46]. Leary *et al.* [47] used the LJ potential to study the structure of the 98-atom clusters.

Baletto, Mottet and Ferrando [48] studied the growth of Ag nanoclusters from a few atoms to about 150 atoms using molecular dynamics (MD) simulations. They found an almost perfect 55 atom icosahedra, 75 atom decahedra and for the cluster size range of around $N = 100$. When $N \approx 100$ the clusters were able to optimize their energy and, for example, the structure for $N = 101$ is decahedral. Baletto *et al.* also studied C_{60} molecules using the Girifalco potential. The results of C_{60} can be compared to other results because C_{60} molecules can rotate freely and so they act as large pseudo-atoms. They found global minima at $N = 13$, 25, 38, 45 and 55. There are close-packed structures for sizes of 38 and 45 atoms [49].

Akola *et al.* have used BO-LSD-MD to study the structure, electronic structure and ionization potential of aluminum clusters with 2–23 atoms [43] and to study structural and electronic properties of small magnesium clusters [50]. Akola *et al.* have also studied atomic structures and geometries and electronic structures of Al_N^- ($N = 19$–102) clusters via *ab initio* local-density-functional simulations [51]. Aguado *et al.* have used the *ab initio* perturbed ion model to study the structural and energetic properties of $(MgO)_nMg^{2+}$ ($n = 1$–29) cluster ions [52]. Kumar and Car have used the density-functional molecular-dynamics method and the simulated annealing technique within the local-density approximation to study the structure, growth and bonding nature of Mg_n ($n = 2$–13) clusters [42].

2.5 Motivation to study close-packed clusters

The motivation to research close-packed clusters is that most metals (e.g. Al [II, 51, 53]) and rare gases have a close-packed structure in bulk and some metals also in small clusters. For example Yi *et al.* compared ideal 55-atom cuboctahedral and icosahedral structures by Car-Parrinello calculations and found that cuboctahedral structure has a lower total energy for Al_{55} [54]. A further motivation is that a new study made by Calvo and Doye [55] shows that when the pressure is increased FCC structures are favoured over icosahedra and icosahedra are favoured over decahedra.

For small cluster sizes, the surface energy of the cluster, the formation energy due

to structural defects, and the electronic structure in metals [56] cause many different isomers within a small energy range. A proper quantum-mechanical calculation of ground state structure for medium- and large-size molecules is then beyond the capabilities of current computers. The problem is that one needs to carry out these calculations for a number of points in the configurational space, and the number goes up exponentially with the size of the molecule. It is thus important to have good initial guesses for the ground state geometry.

Therefore we used the simplest possible hard spheres model. Our goal was to study clusters in general, not any specific material. We used the pair (PP) and tight binding (TB) potentials for the interactions between the hard spheres and used the FCC lattice with stacking faults for the four directions. Because we used a fixed lattice, we can not describe icosahedral clusters. Instead, hard spheres form close-packed structures such as FCC, HCP and the mixtures of these.

2.6 Monte Carlo and Metropolis algorithm

The Monte Carlo and Metropolis algorithms are used to study the ground state geometry of close-packed clusters with stacking faults. Akola *et al.* have used the same procedure for pure FCC lattice to find the ground state geometry [51].

First the FCC lattice and all possible stacking faults inside a spherical volume were generated. These lattice sites were randomly populated so that atoms occupying these lattice sites can form an FCC or HCP lattice or any combination of these two, including stacking faults in all possible directions.

Next, the Metropolis algorithm were used to vary occupied sites. The lattice sites are randomly populated with N atoms, such that the minimum distance between any atom pair is twice the hard sphere radius, i.e., the nearest neighbor distance in the FCC lattice. The starting point was an atomic configuration, A_0, which was updated by selecting one of the atoms randomly and moving it to a different place so that the new atomic configuration is A. Then the energy difference (=difference between coordination number) $\Delta E = E(A) - E(A_0)$ was calculated. If $\Delta E \geq 0$, A is accepted as a new atomic configuration. If $E(A) - E(A_0) < 0$, the configuration A, with a probability $e^{-\Delta E/k_B T}$, is accept. The acceptance is carried out by selecting a random number γ and if $\gamma < e^{-\Delta E/k_B T}$ the configuration A is accepted. A is then set as the initial configuration and the whole cycle is repeated. In Metropolis algorithm, undesirable configurations are also accepted, as they help us to find absolute minima. Many iterations were performed to maximize the coordination number. These procedures were repeated several times to avoid local minima.

We have studied a large set of isomers for each cluster (except for the smallest sizes and $N = 38$). We took into account isomers of the same maximized coordination number. This procedure results in large (111) facets for each of the clusters, as the coordination number for (111) facets is bigger than that for (100) facets and therefore the surface energy is lower for (111) facets.

We used two models for the contact interactions between hard spheres. In the pair-potential model the energy was calculated directly from the coordination number. The second model was based on the tight-binding approximation. In this model the energy of an atom has a square root dependence of the coordination number. In the PP model the energy is calculated as

$$E_{\mathrm{PP}} = -\frac{V}{2}\sum_{i}^{N} C_i = -V N_{\mathrm{bonds}} \tag{2.2}$$

where C_i is the coordination number of atom i, V is the strength of the interaction (V determines the energy scale) and N_{bonds} is the total number of bonds (contacts between the hard spheres). The second model is derived from tight-binding theory [57, 58] and has a simple square root dependence on the coordination number

$$E_{\mathrm{TB}} = -\frac{V}{2}\sum_{i}^{N} \sqrt{C_i}. \tag{2.3}$$

In practice, Eq.(2.3) has shown to be a good approximation for the true TB energy of small clusters. Häkkinen *et al.* have shown that the square-root dependence of the coordination number closely follows the weighted, averaged energy curve [59]. The difference is so small, that this approximation can be used to study our different isomers and it helps us to determine whether there is a difference between different isomers. Nevertheless, this model cannot describe effects related to the details of the electronic structure, such as Jahn-Teller deformation, and the geometries obtained from Eq.(2.3) should not be confused with the most stable geometries determined with the true tight-binding method [60, 61]. The Jahn-Teller theorem [62] says that if the degenerate set of electronic states are partially occupied, the symmetry of the shape is broken and therefore the total energy is lowered. This was first noticed in metal clusters by Clemenger [63].

Clusters can have many different geometries with the same coordination number and consequently the same energy in the PP model. Particularly, there are many isomers with stacking faults. The TB interaction is more sensitive to the energy difference between different isomers. In most cases it totally removes the degeneracy of many ground state isomers of the pair-potential model because the TB model favours geometries where each atom has a similar coordination number. The PP model, however, does not care how the bonds are distributed.

2.7 Results

2.7.1 Geometries of the hard sphere clusters

We have determined the low energy geometries of hard sphere clusters up to $N = 110$ using both the pair-potential and tight binding methods. A detailed discussion of the structure evolution of small hard sphere clusters has been given in Ref. [II] and here we concentrate on clusters with interesting structures.

Starting from a cluster size of $N = 8$ there are many different structures, as HCP structures with n atoms in the FCC-basis and m atoms in HCP-places can arrange atoms in a large variety of ways so that the coordination number is constant. The first cluster size where three different domains of structures where observed with the same coordination number was for $N = 13$. The energetically best structure in our simulation is the FCC structure, as icosahedral structures are not observed using our methods. The lowest-energy FCC structure consists of three fused octahedra and can

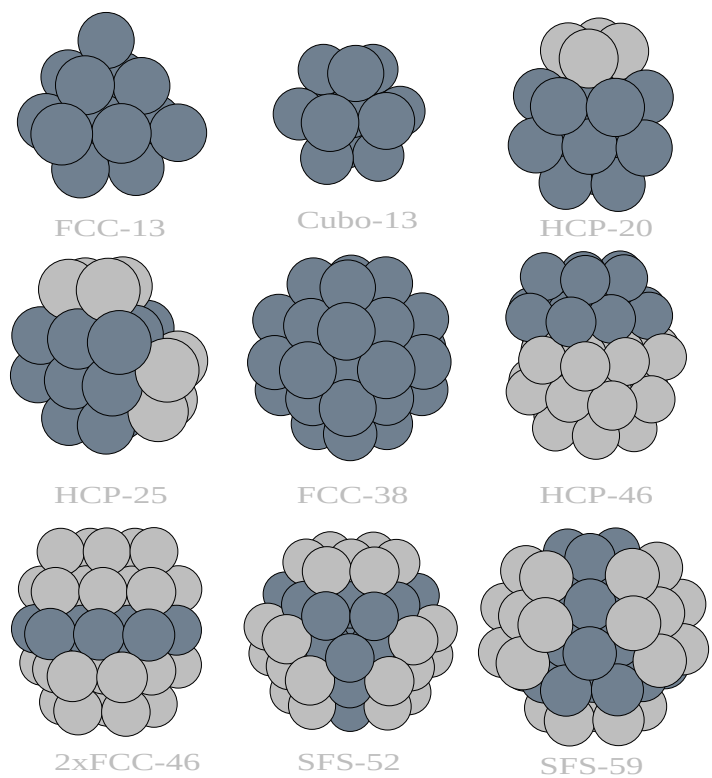

Figure 2.3: The low energy geometries of selected clusters in size region $N = 13$–59. The different shading of layers illustrates changes in packing (stacking faults).

be described by two layers. The energy of this structure is lower than the energy of cuboctahedron structures, although cuboctahedron and the corresponding HCP structure, where the uppermost layer is turned 180 degrees, have a higher symmetry.

The cluster size $N = 20$ is the first size where structures were found to have an FCC basis of three layers and one layer in an HCP configuration. There are new domains of structures in the case of 25 atom clusters: The basis consists of three layers of FCC, On surfaces of this basis there are layers in stacking fault positions as shown in Fig. 2.3.

The clusters sizes $N = 26$–28, 33 and 35 are interesting because in these sizes the FCC structures have smaller coordination numbers than structures with stacking faults. The cluster sizes $N = 38$–40 have the opposite situation: The best and the only structure is the FCC truncated octahedron with additional atoms (0–2 atoms). The 38-atom truncated octahedron is the most stable FCC cluster in the size range we consider. Deaven *et al.* [45] also found the same 38-atom cluster. This structure for $N = 38$ has also been observed in many other studies [23, 46, 47].

In the case of 46 atom clusters two new structures were found. The first structure can be described as a fused FCC and HCP structure where the top two layers of the FCC structures are shared with the bottom two layers of the HCP structure. Fig. 2.3 helps one to visualize this structure. Another structure with the same energy has two FCC parts fused together so that the FCCs share the same layer in the middle of the structure.

For $N = 49$–51, 58–60, 81, 83, 92, 99–100, 105 the most stable PP isomer does not have an FCC structure. An inclusion of the TB model yields the same results qualitatively, the only effect is that isomers with the same coordination number can be separated. The cluster size $N = 50$ is the first cluster size where FCC structures have a smaller coordination number and the difference is two nearest-neighour-bonds instead of one bond. On the other hand, for $N = 86$, 88, 102, and 104 the FCC geometry has more bonds than any of the geometries with stacking faults.

The 55 atom clusters are interesting because this size has been found to be a magic one in many studies. There are two domains of structures in addition to the FCC structure. One of the domains of structures is a combination of the FCC and HCP structures. This kind of structure is the lowest-energy structure for cluster size $N = 55$. The third structure is based on 52 atom SFS [64] structure shown in Fig. 2.3 with three overlayers in stacking fault locations. Akola *et al.* obtained the same result for the Al_{55}^{-} (while the icosahedron is much higher in energy) [51]. The calculations with Lennard-Jones potentials have led to the Mackay icosahedron [23, 46]. Yi *et al.* compared the ideal 55-atom cuboctahedral and icosahedral structures by Car-Parrinello calculations and found that cuboctahedral has a lower total energy for Al_{55} [54].

Clusters with $N = 58$, 59, and 60 are based on a truncated 31-atom tetrahedron with all four overlayers in stacking fault locations. The structure of $N = 59$ is also presented in Fig. 2.3. We denote such isomers with tetrahedral symmetry as SFS. Both the PP and TB models give a large energy difference between the most stable FCC geometry and the SFS ground state.

The FCC structures of cluster size $N = 58$ have a smaller coordination number than structures with stacking faults, so the energies of all FCC structures are higher than the energies of structures with optimized coordination number. The low energy structure is based on a 59 atoms SFS structure with one atom removed. The lowest

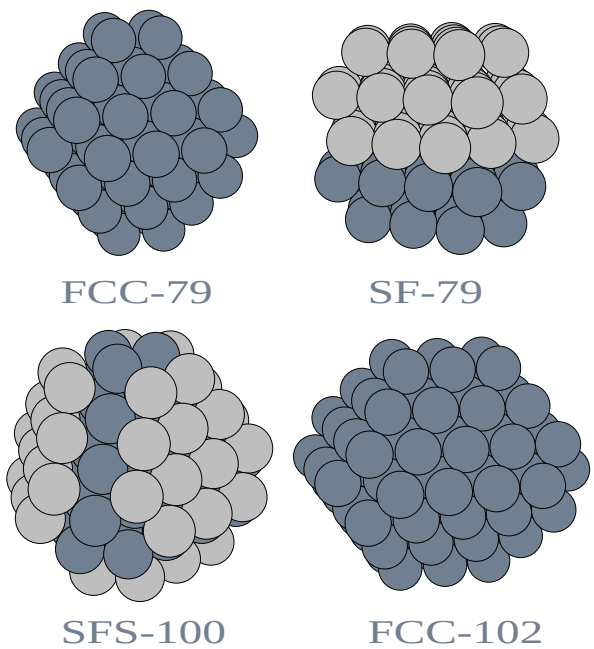

Figure 2.4: The lowest-energy isomers of different cluster sizes in size region $N = 79$–102. The different shading of layers illustrates changes in packing (stacking faults).

energy isomer of $N = 79$ is an FCC structure according to the TB potential with a very small energy difference to the SF structure (structure, which has two FCC units fused together) . The FCC construction of this size gives a complete truncated octahedron (TO). The corresponding SF isomer also has large (111) facets. This gives rise to the lower energy of this structure. Both of these structures are presented in Fig. 2.4. Similar kinds of SF clusters with a stacking fault layer inside the cluster are found for $N = 81-92$, and 94. The clusters with 86 and 88 atoms have nondegenerate FCC energy minima in the PP model. These isomers are based on the FCC-79 with one (111) overlayer.

The most stable isomers for 99 or 100 atoms have an SFS structure based on a

truncated FCC tetrahedron with stacking faults at each of the four surfaces. The 100 atom cluster has the same structural motif as SFS-59, whereas in the case of 99 (101) atoms, one surface atom is removed (added). The lowest-lying TB geometries for $101 \leq N \leq 104$, $N = 106$, 109, and 110 are FCC structures with five (111) layers. They all are related to the FCC-102 structure, which have a full atomic shell configuration (similar to FCC-52).

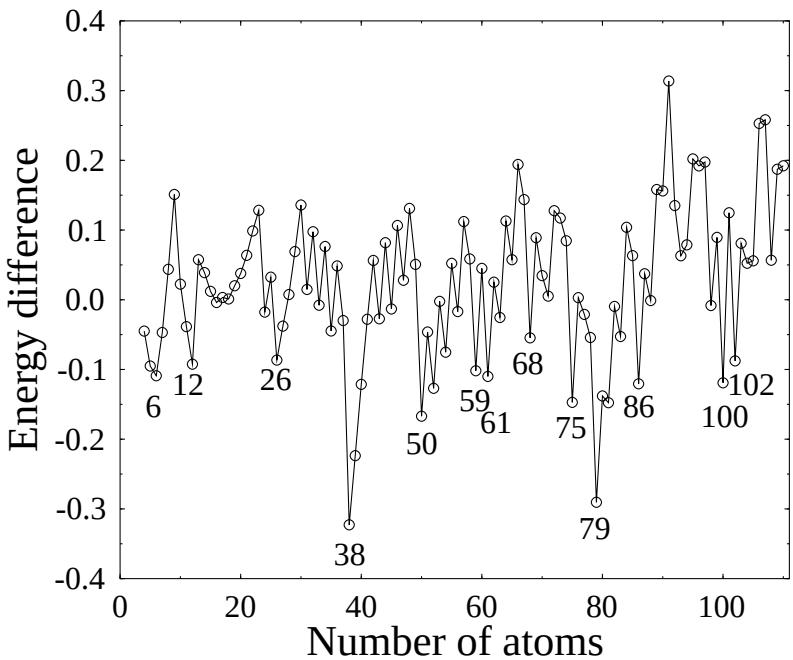

Figure 2.5: Deviation of the lowest energy of TB model.

2.7.2 Magic numbers of hard sphere clusters

The most stable cluster sizes (magic numbers) reflect the stability of the cluster with respect to the neighbouring sizes. In order to see also the possible regions of increased stability, it is convenient to subtract a smooth size dependence from the energy. This can be obtained by fitting the total energies to a "mass formula"

$$E_{\text{ave}} = -E_{\text{coh}}N + bN^{2/3} + cN^{1/3}, \tag{2.4}$$

where b and c are fitting parameters and E_{coh} is the cohesion energy of the model in question ($E_{\text{coh}} = -6V$ for the PP model and $-V\sqrt{3}$ for the TB model) [65, 66]. The first term of (2.4) is the so-called volume term which depends linearly on the size of

the system. The second term represents the energy associated with the surface of a cluster. The last term is related to the curvature of the surface of a cluster.

Figure 2.5 shows the deviation of energy from this function. In the calculations we fixed the first coefficient to the bulk value $a = -6$ ($a = -\sqrt{3}$) and obtained the best fit with $b = 7.651$ and $c = -0.250$ ($b = 1.160$ and $c = 0.369$). The most pronounced local minima are marked in Fig. 2.5, but there are also several weaker local minima. The results also show odd-even alternation in some regions. However, since this behavior is not of electronic origin [67], the minima can be even (for N around 38) or odd (N around 61).

The general profile of the energy curve is related to the total number of bonds. This is natural in our model, which neglects the internal strain. In all the cases, the lowest PP and TB structures have the same number of bonds and qualitatively similar energy curves. Note that only those with magic sizes with 38, 75, 79, 86, and 102 atoms are pure FCC clusters, the rest have stacking faults.

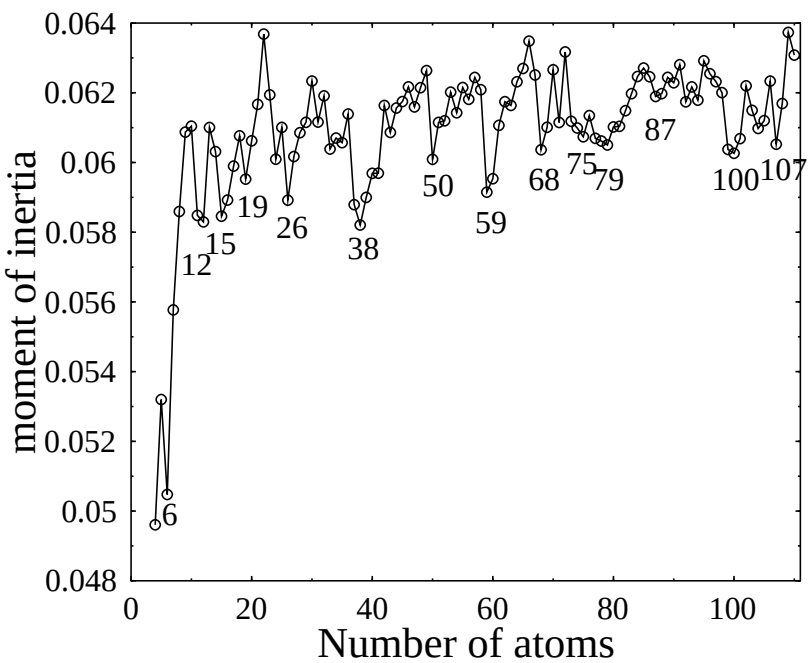

Figure 2.6: The normalized average moments of inertia as a function of the cluster size.

2.7.3 Moments of inertia

The overall shape of clusters is studied by calculating the three moments of inertia for the principal axis, and the normalized average moment of inertia

$$I = \frac{1}{N^{5/3}} \sum_{i}^{N} (\mathbf{R}_i - \mathbf{R}_{\mathrm{cm}})^2, \tag{2.5}$$

where $\mathbf{R}_i$ is the atom position and $\mathbf{R}_{\mathrm{cm}}$ the center of mass (in units of the FCC lattice constant). The factor $1/N^{5/3}$ is chosen because the moment of inertia is proportional to $N^{5/3}$ for a spherical cluster. The normalized moments of inertia are shown in Fig. 2.6, and the similarity between Fig. 2.5 and 2.6 is noticeable. The minima of the moments of inertia are also present in the energy curve. The exceptions are $N = 15$, 19, and 107.

It is also interesting to resolve the cluster deformation on the basis of the moments of inertia, since for a sphere (or a cube) all the principal components of inertia are equal. If the difference between the maximum and minimum components are calculated as a function of the cluster size it is seen that many of the magic clusters ($N =$ 38, 59, 68, 79, 100) have high symmetry, but some (e.g. 50, 86, and 102) have a marked deformation. The large (111) facets compensate for the increase in surface area (deformation) in such cases.

3 Melting of sodium clusters

The melting transitions are among the most studied thermodynamical phenomena. Today, the melting temperatures are well known for nearly all elements. In bulk the melting transition happens abruptly at a single temperature and is associated with the latent heat of fusion. The latent heat of fusion is needed to destroy the regular solid structure. This means, that energy can be added to the system at the melting temperature without increasing the temperature. The temperature starts to rise again upon addition of energy only after the system has become completely liquid.

Thermodynamic properties are accurately defined only for systems with an infinite number of atoms. The relative fluctuation of a thermodynamic property is proportional to $1/\sqrt{N}$, where N is the average number of particles in the system. Now when N decreases, the fluctuations in the system become significant and evaluation of the accurate value of any observable becomes more difficult. This is the problem with small particles such as atomic clusters.

3.1 Background

Usually clusters melt at temperatures lower than the bulk material because of their high proportion of surface atoms with reduced binding energy. This has been observed both in theoretical simulations [68, 69, 70] and in experiments [71, 72, 73, 74]. Exceptions also exist: Shvartsburg and Jarrold [75] demonstrated that small tin cluster ions with 10-30 atoms remain solid above the melting temperature of bulk tin. Nevertheless, in general, as the cluster size decreases, the melting temperature and latent heat of fusion per atom decreases and the melting transition region widens [74, 76]. For example, the melting temperature of tin clusters systematically decreases as the size of the cluster decreases from 50 to 5 nm (Fig. 3.1)[74].

Rytkönen *et al.* [68] estimated the melting temperatures for sodium clusters in the size range $N = 8 - 55$ using an *ab initio* simulation method and they found that they decrease nearly monotonically as a function of size. However, because almost all sizes studied were electronically magic, these calculations do not exclude the possibility for nonmonotonical behavior. There is indeed an evidence indicating that the melting temperatures of sodium clusters do not vary monotonically with cluster size for small clusters (< 350 atoms) [76, 77, 78, 79]. Nonmonotonical melting temperature variation

has also been observed in a theoretical study of argon clusters [80].

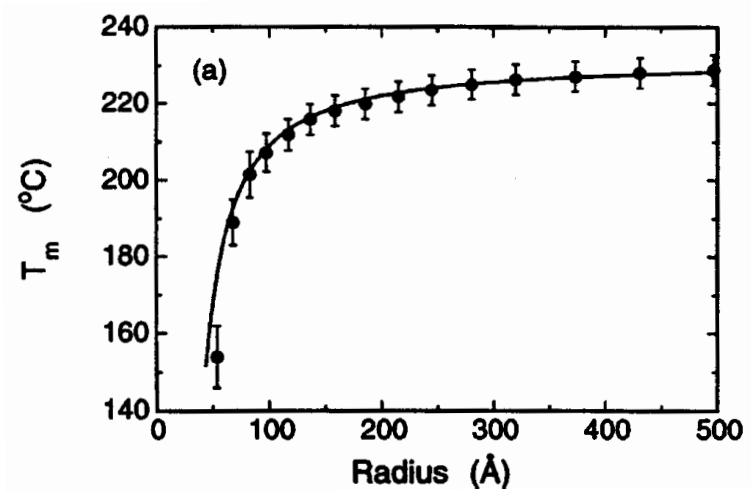

Figure 3.1: The melting temperatures of Sn particles as a function of the size [74].

The melting transition of a finite cluster does not occur at a well defined temperature as it does in the bulk material. Instead, the melting transition spreads over a finite temperature range which broadens as the cluster size decreases [81]. The freezing temperature T_f is generally defined to be the lower end of the melting temperature range below which the cluster is completely solid and, respectively, the upper end of the range defines the melting temperature T_{melt} above which the cluster is completely in the liquid phase. However, the experimental or theoretical determination of T_f or T_{melt} is not straightforward and other definitions for the solid and liquid state are used. For example, Rytkönen *et al.* defined the liquid cluster such that if a certain percentage (20 %) of the nearest neighbours of an atom had moved away within a small time intervall, then this cluster was considered as liquid [82].

Between T_f and T_{melt}, clusters show premelting, structural isomerization [76, 83, 84, 85], and dynamical coexistence. The most usual premelting case is surface melting [86, 87, 88, 89]. An ensemble of small clusters in the melting region can be a mixture of solid-like and liquid-like clusters, where the cluster can fluctuate in time between the solid and liquid phases [87, 90, 91, 92, 93, 94, 95, 96, 97].

The liquid clusters differ from the solid ones since they have higher potential energies, larger diffusion coefficients and more disordered structures. In the coexistence region, where both solid-like and liquid-like states may exist, the energy as a function of temperature exhibits an S-shaped curvature. This curve is called the caloric curve and its derivative, $C(T) = \frac{\partial E}{\partial T}$, the heat capacity. In an infinite system the caloric curve has a step at the melting temperature. The height of this step is the latent

heat, which is the energy needed to destroy the lattice at the melting temperature. In a finite system the latent heat can be obtained from the S-curve.

3.2 Determining the melting temperature

There are a number of methods used to detect the melting transition and to determine the melting temperature. One of the first experimental ways to determine the melting temperature was to use a scanning electron-diffraction technique [98], which uses the fact that the diffraction of high-energy electrons by crystalline powders produces patterns of rings that are relatively narrow compared to those obtained from electron diffraction by liquids. The melting point is determined to be at the temperature where the last diffracted beam characteristic to a solid structure disappears. Later, the disappearance of the geometric magic numbers [26] and caloric curve [71, 79, 81] were used to determine the melting temperature. More recently the caloric curve was measured by using photofragmentation. By evaporating atoms with laser and then plotting the intensity of the charged fragments against the number of evaporated atoms one can determine the caloric curve [71, 73, 78, 79, 81, 99] (see 3.8).

Theoretically, we have three different methods for determining the melting temperature. One method is to observe a steep rise in the potential energy versus temperature curve (caloric curve) [69, 72, 74, 82, 100]. The other is to obtain the melting transition by observing the disappearance of the internal symmetry. However, in this case one has to be careful since in the case of clusters the initial geometry could be amorphous making this method unusable. One has to be also aware of structural isomerization. The third method is the use of dynamical properties. For example, the melting temperature of the cluster can be determined from the mean square displacement (MSD) or diffusion coefficient as a function of temperature [69, 76]. According to the Lindemann's criterion [101, 102, 103] melting occurs when the root-mean-square displacement for the atoms in the cluster reaches a critical fraction ($\delta > 0.1$) of the distances between them in a relatively short time. The melting transition can also be determined using a local order parameter, for example, the percentage of configurations where an icosahedron is found inside the cluster [100]. It should be noted that for small systems the melting temperature can be defined in many ways. In some cases the melting temperature has been taken as half the value of the coexistence interval, $\frac{1}{2}(T_f + T_{melt})$ [91], and in some cases as the value near T_{melt} [100].

3.3 Earlier experiments and simulations

The first experimental study of the melting temperatures of sodium clusters was performed by Martin *et al.* [26]. They used the mass spectra of sodium clusters to study the melting temperatures and observed that for sodium clusters bigger than 1000 atoms the icosahedral magic numbers disappear as the temperature is increased. Subsequently, a measurement of the melting temperatures was performed by Haberland and collaborators [71, 79, 81]. The melting temperatures of sodium cluster cations were deduced from caloric curves obtained from photodissociation measurements. According to these measurements, the melting temperature is not a monotonically increasing function of the cluster size (see Fig. 3.2). In particular, the melting temperature for Na_{55}^{+} was found to be higher than that for others in the range $N < 350$. There was also a pronounced peak at $N = 142$.

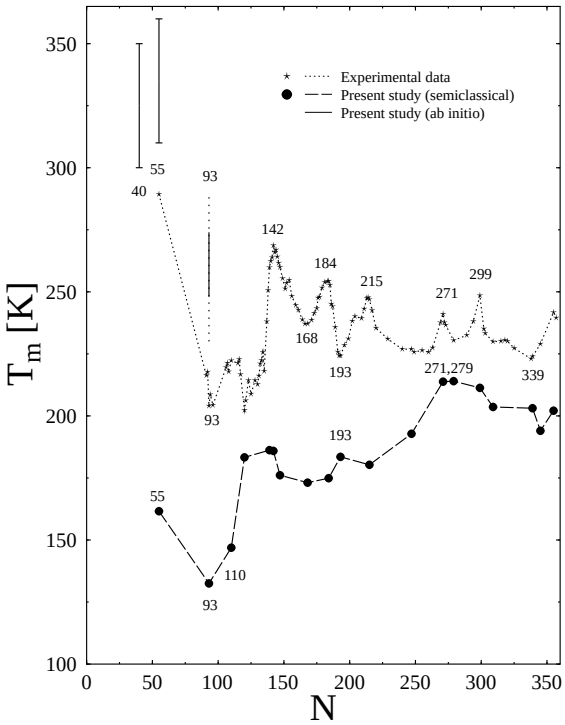

Figure 3.2: The experimental melting temperatures determined using photodissociation measurements [71, 79, 81].

A number of computer simulations on the melting of small sodium clusters has been reported. The major part of the simulations has been performed using phenomenological

interatomic potentials [76, 93, 104, 105, 106, 107, 108]. Others used *ab initio* methods [69, 70, 109, 110, 111] which allow a more realistic treatment, but are computationally much more extensive than the ones performed using phenomenological potentials. For example, Calvo and Spiegelmann [78] employed a classical empirical potential (SMA) and a simple tight-binding model (TB) to study the size range $N = 8$–147. They observed that for clusters with less than 75 atoms both the melting temperature and the latent heat of melting exhibit strong, nonmonotonic variations as a function of size. For large sizes, the transition was found to resemble the bulk solid-liquid phase transition rounded by finite size effects. In this year, Calvo and Spiegelmann new results, which show, in contrary to previous findings, that premelting effects are also present at medium sizes [112]. Rytkönen *et al.* [69] used *ab initio* molecular dynamics simulations to study the dynamics and electronic structure of Na_{55}. The melting transition was observed in the region 300-350 K where the latent heat of melting was 11 meV/atom. Aguado *et al.* [109, 110] performed constant-energy molecular dynamics simulations with the Car-Parrinello technique. Surface melting was observed at ~ 240 K for Na_{142}, homogeneous melting at ~ 270 K, and similarly for Na_{92} at ~ 130 K and ~ 240 K, respectively. Na_{55} was observed to melt in a single stage at 190 K. Blaise *et al.* studied the melting of sodium clusters Na_N^+ ($N = 53$–57, 93, 139, 147) using an *ab initio* within the extended Thomas-Fermi approximation. They found a pronounced maximum in the melting point around $N = 55$ [113].

3.4 Latent heat of fusion, width of phase transition and binding energy

Experimentally it has been observed that the latent heat of fusion decreases from the bulk value as the cluster size is decreased [74]. Molecular dynamics simulations have also shown a steady decrease in the latent heat of fusion with a decreasing cluster size for gold clusters [72]. Kusche *et al.* [81] have studied the variation of the latent heat and they found that the maxima occur near T_{melt}, but not exactly at the same size but seems to be shifted from T_{melt} in the direction of the icosahedral shell closings.

The width of phase transitions in finite systems has not been studied systematically. Imry [114] has shown that the broadening of a first-order phase transition is proportional to the latent heat of the transition. Similar findings were made by Labastie and Whetten [115].

The binding energy has been calculated for small ($2 \leq N \leq 14$) sodium clusters using both *ab initio* and classical molecular dynamics simulations [68]. The binding energy values calculated with the classical model are 0.15–0.20 eV higher than the ones calculated with the *ab initio* method and they also increase monotonically. Rey *et al.*

[116] studied the binding energies of Ni_N, Pd_N, Au_N, and Ag_N clusters ($N = 2 - 23$) on the basis of the embedded-atom model and the second-moment approximation to the tight-binding method using constant-energy molecular dynamics simulations. The calculated binding energies increase monotonically as the size of the cluster increases. Spiegelmann *et al.* [117] came to the same conclusion by using a distance-dependent tight-binding Hamiltonian based on the 3s atomic orbitals for $N = 2 - 40$. Northby [8] pointed out that the most tightly bound Lennard-Jones cluster in the range $13 \leq N \leq 147$ is $N = 135$. This structure is a truncated 147-atom icosahedron without 12 corner atoms. The binding energy differences also show that the binding energy per atom increases linearly for $136 \leq N \leq 147$.

3.5 Electronic and geometric magic numbers

It has been observed experimentally that the peaks in the mass spectrum for large sodium clusters (with more than 1500 atoms) correspond to the Mackay icosahedral shell closings (see Fig. 3.3) [14, 27]. For small sodium clusters, the peaks of the mass spectrum have been observed to correspond to electronic shell closings (2, 8, 18, 20, 34, 40, 58) (see Fig. 2.2) [73] and were first observed by Knight *et al.* [13]. The electronic magic numbers can be observed up to at least 3000 sodium atoms at high temperatures [118]. At low temperatures the electronic shell structure becomes less important compared to the geometrical shell structure for sizes near $N = 2000$ [119].

Magic numbers based on electronic shells are now well understood in the framework of the self-consistent spherical jellium model, which is explained in Chapter 4. Because of the electronic contribution, the binding energy per atom reaches a maximum at electronic shell closings [119]. However, the large fluctuations in the experimentally determined melting temperatures are not correlated with either electronic or geometric shell closings, and consequently the fluctuation in the melting temperature against the number of atoms cannot be directly explained in terms of either of them.

3.6 Ionization potential

The ionization potential is the energy needed to take one electron out of the cluster. Sodium clusters which have a complete outer shell of atoms have a slightly higher ionization potential than those with an incomplete shell and they (closed shell structures) show a minima in the mass spectrum [27]. The closed-shell clusters have high ionization energies because the ionization energy is decreased in clusters with incomplete shells by the creation of an electric dipole moment [27]. Electric dipole moments are

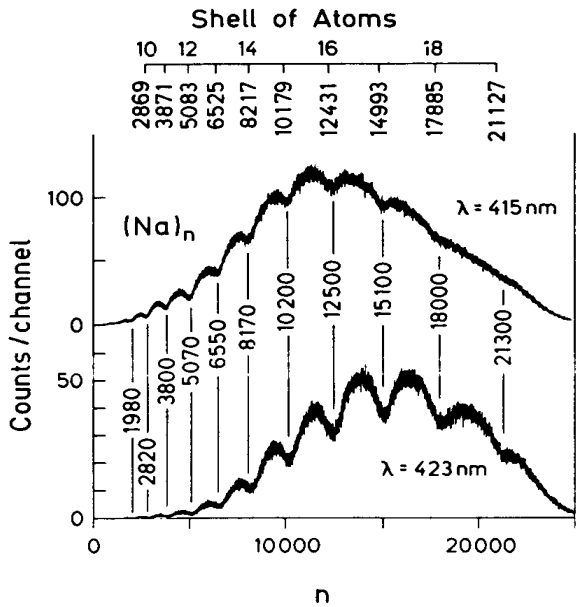

Figure 3.3: Averaged mass spectra of sodium clusters according to Ref. [14]. Minima occur at values of N corresponding to the total number of atoms in close-packed cuboctahedra and icosahedra. The values are listed at the top of the diagram.

also caused by the presence of steps on the clusters surface. The theoretical ionization potential is calculated from the energy difference between the neutral and positively charged clusters. The second ionization potential is the energy needed to remove one electron from the cation.

3.7 Negative heat capacity

Under certain conditions an increase in energy can lead to a lower temperature, i.e. the heat capacity is negative. Negative heat capacities have been known in astrophysics [120] where energy can be added to a star which then cools down. Labastie and Whetten have also observed negative heat capacities in atomic clusters [115]. Negative heat capacity in clusters occurs because the cluster converts some of its kinetic energy into potential energy to avoid partly molten states. As the kinetic energy does not remain constant there is a possibility that the cluster can cool altough its total energy is increasing.

Michaelian *et al.* [108] have studied the heat capacities of Na_{13}, Na_{20}, Na_{55}, Na_{135}, Na_{142} and Na_{147} clusters using a many-body Gupta potential and microcanonical molecular dynamics simulations. Negative heat capacities around the cluster melting-

like transition were obtained for $N = 135$, 142 and 147, but the smaller clusters ($N = 13$, 20 and 55) did not show this peculiarity.

The first experimental evidence of negative heat capacity of atomic clusters was measured by Schmidt *et al.* [121] using the same experimental method as described in the next section (3.8).. They have shown that a cluster containing exactly 147 sodium atoms has a negative heat capacity near its solid to liquid transition. At the melting temperature an increase of the internal energy of Na^{+}_{147} by 1 eV leads to a corresponding decrease in temperature by about 10 K. We have not observed negative heat capacities in our *ab initio* simulations. However, our cluster sizes are smaller than those where negative heat capacity was observed.

3.8 One of experimental methods

Haberland *et al.* have used the so called cluster calorimetry method [71, 73, 81, 99, 122, 123] to measure the energy distribution of clusters of a certain size and temperature. The cluster calorimetry method consists of two steps as shown in Fig. 3.4. First, the clusters of a certain size and temperature T are formed. The cluster ions are produced and thermalised in a heat bath and after that a mass spectrometer is used to select a single cluster size. During the second step the size selected clusters are irradiated by a laser beam and clusters absorb several photons. The distribution of the charged fragment ions caused by the evaporation of atoms is measured by a second mass spectrometer. Since the fragments are caused by absorbtion of photons, the energy of the photon is seen from the distance between two different distributions of the fragment ions. This allows one to calibrate the mass scale in terms of energy [71, 73, 121]. The intensity of the charged fragments is plotted against the number of evaporated atoms. The energy E of a free cluster can now be obtained from its photofragmentation mass spectrum. Because we know the energy and temperature, the caloric curve $E = E(T)$ can be constructed.

3.9 Theoretical methods

The thermodynamical properties of clusters can be calculated using simulations based on the Monte Carlo (MC) or molecular dynamics (MD) methods. Molecular dynamics requires solving Newton's classical equations of motion numerically starting from a given initial configuration and initial velocities of the atoms and then using a finite time step, δt, to evolve the system. The MC method is a statistical way of calculating the averaged values of the system, but we did not use this method in our melting calculations.

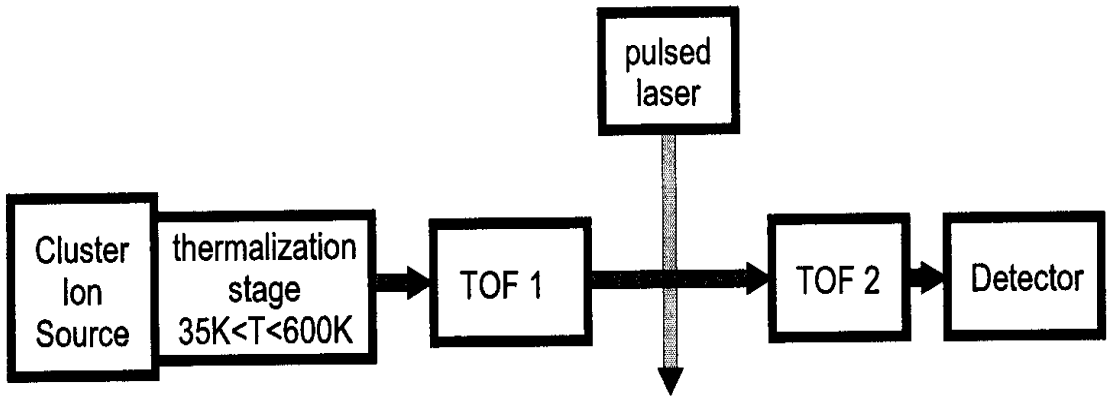

Figure 3.4: Schematic depiction of the cluster calorimetry method [71, 79, 81]. TOF1 and TOF2 are the time-of-flight mass spectrometers.

The molecular dynamics method based on a model interaction between the atoms is widely used in the treatment of dynamical problems of classical statistical physics because of its high efficiency. However, if interatomic interactions have to be determined from the electronic structure, one needs a different approach. This is the so called *ab initio* dynamics.

In *ab initio* methods the electronic degrees of freedom in the system use fully quantum mechanical models. Obviously, when the number of electrons is increased the calculations quickly become very large and therefore approximations must be made. The interactions in the system can be calculated from the interaction of the valence electrons among themselves and from the classical electrostatic interaction between the ionic cores and the valence electrons. In this way, the Hamiltonian for the system is reduced just enough to be able to solve the dynamical evolution of the system for a finite time interval.

3.9.1 Molecular dynamics simulation method

For the molecular dynamics simulations of the ensemble of atoms we use the velocity Verlet algorithm [124] for the time-integration of the equations of motion. The new coordinates $r_i(t+\Delta t)$ and velocity $v_i(t+\frac{1}{2}\Delta t)$ are calculated from the old coordinates $r_i(t)$, velocities $v_i(t)$ and accelerations $a_i(t)$ as follows:

$$r_i(t+\Delta t) = r_i(t) + v_i(t)\Delta t + \frac{1}{2}a_i(t)(\Delta t)^2, \tag{3.1}$$

$$v_i(t+\frac{1}{2}\Delta t) = v_i(t) + \frac{1}{2}a_i(t)\Delta t. \tag{3.2}$$

When the new coordinates are known, the new forces F_i on the atoms and the new accelerations are calculated using

$$a_i(t+\Delta t) = \frac{F_i(t+\Delta t)}{m_i}, \tag{3.3}$$

where m_i is the mass of atom i. Finally, the new velocities can be calculated at time $t+\Delta t$ from

$$v_i(t+\Delta t) = v_i(t+\frac{1}{2}\Delta t) + \frac{1}{2}a_i(t+\Delta t)\Delta t. \tag{3.4}$$

Molecular dynamics methods can use both the canonical and microcanonical ensembles. For the microcanonical ensemble the total energy of the system is constant, but in the canonical ensemble the temperature of the system in constant using some appropriate thermostat. The most commonly used thermostat is the Nośe-Hoover thermostat [125]. In this method the acceleration of the ith atom in an N atom system at time t is given by

$$a_i(t) = \frac{F_i(t)}{m_i} - \xi(t)v_i(t), \tag{3.5}$$

where $\xi(t)$ is the thermodynamic friction coefficient of the Nośe-Hoover thermostat. $\xi(t)$ is determined by

$$\frac{d\xi}{dt} = \frac{T(t)-T_{ref}}{\tau^2 T_{ref}}, \tag{3.6}$$

where T is the instantaneous temperature at time t, T_{ref} is the desired average temperature, and τ is the relaxation time of the thermostat. The time-evolution of the coefficient ξ is iterated during the simulation.

The kinetic temperature is calculated from the kinetic energy, E_k by

$$T_k = \frac{2E_k}{(3N-6)k_B} \tag{3.7}$$

where E_k is the mean value over the whole trajectory, N is the total number of atoms and k_B is the Boltzmann constant. This equation is exact in the canonical ensemble, but T_k differs from the thermodynamic definition of temperature in the microcanonical ensemble [126].

For our simulations, we chose an empirical many-body potential

$$V = -\sum_{i=1}^{N}\left\{\sqrt{\sum_{j=1\neq i}^{N}\zeta_0^2\exp\left[-2q\left(\frac{r_{ij}}{r_0}-1\right)\right]} - \sum_{j=1\neq i}^{N}\epsilon_0\exp\left[-p\left(\frac{r_{ij}}{r_0}-1\right)\right]\right\}, \tag{3.8}$$

where $\epsilon_0 = 15.956$ meV, ζ_0=291.14 meV, r_0=6.99 a_0, q=1.30 and p=10.13. The equation and these parameter values are those given by Li *et al.* [127]. The square root

dependence in Eqn. (3.8) comes from tight binding theory and it has been found to describe fairly well the energies of clusters and surfaces [59]. The parameter p is related to the Born-Mayer potential and the parameter q to the attractive interaction representing the band structure. This method, based on the many-atom potential, is known as semi-classical molecular dynamics. We used a time step 5 fs and a time constant in the Nośe-Hoover thermostat $\tau = 25$ fs. The system was run for 0.5 ns to achieve equilibrium at a specific temperature and 5 ns for extracting the data. The parameter pairs $p = 20.26$, $q = 1.30$ and $p = 10.13$, $q = 2.60$ were also used to see how a change in the parameters of a potential affects the melting temperature.

3.9.2 Ab initio molecular dynamics

The most important idea in quantum mechanical molecular simulations is the Born-Oppenheimer approximation according to which the Schrödinger equation can be separated into parts: the motion of the ions and the motion of the electrons. The motion of ions is treated classically. The forces acting on the nuclei are computed from electronic structure calculations. The electronic many-body problem can be solved using the Kohn-Sham method with the local density approximation [128]. The interaction between the valence electrons and the ionic cores is weak in metals and in metallic clusters because of the effective screening of the nuclear charge by the tightly bound core electrons. This is why the electron-ion interaction can be formulated in terms of pseudopotentials.

Born-Oppenheimer local-spin-density molecular dynamics

The *ab initio* calculations made in this thesis were performed using a Born-Oppenheimer local-spin-density molecular dynamics (BO-LSD-MD) simulation method devised by Barnett and Landman [129]. According to the Born-Oppenheimer approximation only the nuclei behave like classical particles, whereas the electrons are treated as quantum objects [130]. In the Born-Oppenheimer method the electronic structure is solved after each molecular dynamics calculation time step, where the set of nuclear positions is fixed for that instance of time. This reduces to solving the time-independent Schrödinger equation. The gradients of the resulting total electronic energy with respect to the ionic positions give the forces acting on nuclei, which are treated classically. This infers that the time-dependence of the electronic structure is a consequence of nuclear motion.

If the ions and valence electrons of the system are on the Born-Oppenheimer potential-energy surface the total energy of the system is the sum of the ground-state energy of the valence electrons, the ionic kinetic energy and the interionic interaction energy.

In the Born-Oppenheimer approximation the wave function is separated into two independent parts

$$|\Psi\rangle = |\Psi_{electron}\rangle \cdot |\Psi_{nuclei}\rangle. \tag{3.9}$$

To calculate the ground-state electronic energy the method uses the Kohn-Sham formulation with local-density approximation (LDA). The ground-state energy of the valence electrons is calculated by an approximation where the ground-state electron energy is the sum of the kinetic energy of electrons, the electron-ion interaction energy and the electron-electron interaction energy

$$E_{electron} = E_{kin} + E_{eI} + E_{ee}. \tag{3.10}$$

The wave functions can be calculated from the Kohn-Sham equation (in atomic units)

$$\{-\frac{1}{2}\nabla^2 + V_\sigma(\rho_+, \rho_-)\}\Psi_{j\sigma} = \epsilon_{j\sigma}\Psi_{j\sigma}, \tag{3.11}$$

where σ is the spin index. The electronic density for the corresponding spin index is

$$\rho_\sigma = \sum_j f_{j\sigma}|\Psi_{j\sigma}|^2, \tag{3.12}$$

where the $f_{j\sigma}$ are the occupation numbers and $\sum_{j,\sigma} f_{j\sigma} = N_{electron}$, and $N_{electron}$ is the number of valence electrons.

The functional derivative of the electronic energy gives the Kohn-Sham potential operator

$$V_\sigma = \frac{\delta E_{electron}}{\delta \rho_\sigma}. \tag{3.13}$$

The potential energy must be obtained self-consistently, because it depends on the electronic density.

The kinetic energy of electrons using Kohn-Sham wave functions can be calculated from

$$T_{kin} = \sum_{j,\sigma} f_{j\sigma}\langle j\sigma|\hat{T}|j\sigma\rangle, \tag{3.14}$$

where the kinetic-energy operator is $\hat{T} = -\frac{1}{2}\nabla^2$. To calculate the electron-ion interaction the nonlocal pseudopotentials are needed. The electron-ion interaction can be calculated from

$$E_{eI} = \sum_{j,\sigma} f_{j\sigma} \sum_I \langle j\sigma|\hat{V}_I|j\sigma\rangle, \tag{3.15}$$

where the nonlocal $\hat{V}_I$ is obtained from a semi-local pseudopotential. In the pseudopotential the ionic core is described by an average pseudopotential of nucleus and core electrons. The use of pseudopotentials make it possible to describe explicitly the

valence electrons and this determines the physical properties of the atoms. Now the nonlocal norm-conserving pseudopotential can be used [131].

Pseudopotentials are required to produce pseudo-wave-function (see below) solutions that approach the full wave function outside a core i.e., in the "chemical region" where the interatomic bonds are formed. Inside the core the pseudopotential and the wave function should be as smooth as possible, in order to allow for a small plane wave-cutoff.

The electron-electron many-body interaction is obtained from

$$E_{ee} = \int d^3r[\rho_+(\vec{r}) + \rho_-(\vec{r})][\epsilon_H(\vec{r}) + \epsilon_{xc}(\vec{r})], \tag{3.16}$$

where $\epsilon_H(\vec{r})$ is the Hartree energy functional and $\epsilon_{xc}(\vec{r})$ is the exchange-correlation energy functional.

If the LDA is used, the exchange-correlation energy functional depends only on the total density and is simply the exchange-correlation energy per electron of a uniform electron gas with density $\rho(\vec{r}) = \rho_+(\vec{r}) + \rho_-(\vec{r})$. Another possible approximation is based on gradient corrections, where the exchange-correlation energy functional also depends on the density gradients. The gradient corrections take longer to calculate than the LDA, but gives more accurate total and binding energies, ionization potentials and electron detachment energies.

The BO-LSD-MD uses the plane-wave basis set in the calculation of the ground state of the electronic energy of a finite system. In this method the wave function $\Psi_{j\sigma}(\vec{r})$ is expanded in a plane-wave basis within the calculation boundaries, or cell,

$$\Psi_{j\sigma}(\vec{r}) = \Omega^{-1/2} \sum_g \widetilde{\phi}_{j\sigma}(g) e^{i\vec{g}\cdot\vec{r}} \tag{3.17}$$

where $\Psi(\vec{r})$ has a finite value inside the cell and zero outside the cell. Ω is the volume of the cell, $\widetilde{\phi}_{j\sigma}(\vec{g})$ gives the coefficients of the plane-wave expansion and $\vec{g}$ is the reciprocal-space grid. This method uses a dual-space formalism, that is the calculations are carried out using both real and reciprocal spaces. Because the wave function is zero outside the cell, the amplitude and the gradient of the plane-wave functions have to vanish outside the cell.

The evaluation of the force on each ion can be calculated from the gradient of the Hamiltonian matrix elements

$$\langle j\sigma|\hat{H}|k\sigma\rangle = \sum_g \widetilde{\phi}_{j\sigma}(-\vec{g})\widetilde{\phi}'_{k\sigma}(\vec{g}) \tag{3.18}$$

using the Hellman-Feynman theorem. According to the Hellman-Feynman theorem the forces which act on nuclei are derivable from the classical potential and the electronic wave function.

In the case of sodium the full electronic structure calculation is done explicitly for the sodium $3s^1$ electrons. The calculation of the various terms is performed either in real space or in its dual space, depending on which one of the methods is more efficient.

Car-Parrinello method

The Car-Parrinello method is an *ab initio* molecular-dynamic method [132, 133, 134, 135, 136, 137] in which the electrons are treated explicitly. The total energy of a cluster is written as a functional

$$E[\Phi_i, R_I] = \sum_{i=1}^{N} \langle \Phi_i | -\frac{1}{2}\nabla^2 | \Phi_i \rangle + U(\Phi_i, R_I), \tag{3.19}$$

where

$$U(\Phi_i, R_I) = \sum_{i=1}^{N} \langle \Phi_i | \left[-\sum_{A=1}^{N} \frac{Z_A}{r_{iA}} + \sum_{j>i}^{N} \frac{1}{r_{ij}} \right] | \Phi_i \rangle + \sum_{A=1}^{M} \sum_{B>A}^{M} \frac{Z_A Z_A}{R_{AB}}. \tag{3.20}$$

The total energy depends on the Kohn-Sham orbital functions Φ and the coordinates R_I of the ions. If Φ and R_I are treated as independent degrees of freedom, the variational principle applied to the total Lagrangian of the system leads to the equations of motion

$$\mu \frac{\delta^2 \Phi_i}{\delta t^2}(r,t) = -\frac{\delta}{\delta \Phi_i^\star(r,t)} E(\Phi_i, R_I) + \sum_k \lambda_{ik} \Phi_k(r,t), \tag{3.21}$$

and

$$M_I \frac{\delta^2 R_i}{\delta t^2} = -\nabla R_I E(\Phi_i, R_I), \tag{3.22}$$

where M_I are the masses of the ions, μ is a fictitious mass of the electronic degrees of freedom and the Lagrange multipliers λ ensure the orthonormalisation of the Kohn-Sham orbitals [130].

Comparison between BO-LSD-MD and Car-Parrinello method

The success of BO-LSD-MD method is based on the method that enables the system to stay on the Born-Oppenheimer energy surface at each time step. This method makes it possible to use a relatively long time step, typically around 1–10 fs. The length of the time step is limited only by the vibrational time scale of ions and the performance of the integration algorithm. The BO-LSD-MD method has been used successfully in the study of various problems including melting, structures, ionization potential etc. [43, 68, 69, 138, 139] for metal clusters.

In the Car-Parrinello method [132, 140], the equations of motion for the ions and valence electrons are coupled. The explicitly treated electron dynamics limits the largest time step that can be used to integrate simultaneously the coupled equations of motion for nuclei and electrons. Accordingly, this method requires a very short time step, typically 10^{-16} s, which is 10 times smaller than what can be used in the BO-LSD-MD method. In both methods the time-steps used are relatively small and therefore they cannot be used to simulate long-lasting effects. Also, the selection of time step is important since a too long time step can lead to numerical instabilities.

The difference in the time step lengths does not mean that the BO-LSD-MD method is 10 times faster than the Car-Parrinello method. It should be noted that an other difference between the methods is that in the Car-Parrinello method the expectation value of the electronic Hamiltonian is not minimized after each time step as it is in the case of BO-LSD-MD. Therefore, in the Car-Parrinello method, full self-consistency is not required as it is in BO-LSD-MD. The accurate treatment of the electronic LSD Hamiltonian is necessary for BO-LSD-MD, but in the case of Car-Parrinello it is only needed at the very first step in order to obtain the initial wave function. When these two things are considered, the Car-Parrinello method is, in practice, a little faster. The BO-LSD-MD can be made as fast as the Car-Parrinello method, but at the expense of energy conservation.

3.10 Results

3.10.1 Semi-classical simulations

Semi-classical simulations were performed for selected clusters over the range $N = 40$–355. The cluster sizes were selected so that they correspond to the local minimum or maximum values of the experimentally determined melting temperature as a function of cluster size [71, 79, 81].

The initial configurations for all the simulations were based on icosahedral packing. Nonmagic clusters were prepared by removing surface atoms from a complete icosahedron. Since no global optimization was performed it is likely that the starting geometries for cluster sizes, with more than 150 atoms, were not the ground state geometries. Also, in this size region there are usually several quite different geometries within a small energy interval. We used icosahedral starting geometries in our simulations since we knew that our model potential favours ground state geometries that are similar to the complete icosahedra.

Several constant-temperature molecular dynamics simulations were performed for each

cluster size to obtain the caloric curve. The total and potential energy as well as the heat capacity were used to analyze the transition from solid to liquid phase. The melting temperature of a cluster was defined to be at the temperature where the heat capacity curve attains its maximum value.

For each cluster size we determined the energy of the cluster versus its temperature. Because of the limited number of simulations for a single cluster and the statistical fluctuation of energy, we fitted a monotonous function to the simulation data. The total energy at any temperature in the ensemble was estimated by

$$E_{tot}(T) = f(T)E_{sol}(T) + [1 - f(T)] * E_{liq}(T) \tag{3.23}$$

where

$$E_{sol}(T) = a_{sol} + b_{sol}T \tag{3.24}$$

$$E_{liq}(T) = a_{liq} + b_{liq}T \tag{3.25}$$

and $f(T)$ is given by

$$f(T) = \frac{1}{e^{(T-T_0)/c} + 1}. \tag{3.26}$$

$f(T)$ and $1 - f(T)$ represent the fraction of time spent in the solid-like and the liquid-like phases, respectively. Because the E_{tot} curves for the solid-like and the liquid-like phases were assumed to be linear outside the coexistence range, a least-squares fit gives the constants a_{sol}, b_{sol}, a_{liq}, b_{liq}, T_0 and c. The parameter c measures how abrupt the transition is, and T_0 is related to the maximum point of the heat capacity. The heat capacity can be directly extracted by taking the derivative of the analytic function E_{tot}. The melting temperature T_m is the temperature where the heat capacity attains its maximum value. Our method is thus analogous to the one employed by Schmidt *et al.* [73, 79]. The values of the latent heat of fusion have been obtained by extrapolating the lines corresponding to solid-like and liquid-like phases Eqs. (3.24) and (3.25) to the region between these two phases and then determining the energy difference between these lines at $T = T_m$, i.e.

$$E_{LH} = E_{sol}(T_m) - E_{liq}(T_m) \tag{3.27}$$

All cluster sizes except for Na_{40} satisfy the equation for $E_{tot}(T)$ Eq. (3.23) quite well. Because the melting temperature region of Na_{40} is fairly broad, the simulated data does not fit to Eq. (3.23). For sizes larger than 193 atoms, the caloric curves show a small increase near the freezing temperature T_f. The reason for this is most likely surface melting, which has also been observed in large clusters [100].

The experimental [71, 79, 81] and semi-classical melting temperature of sodium clusters are presented in Fig. 3.5 as a function of cluster size. Our semi-classical results show the maxima of the melting temperature at cluster sizes $N = 55$, 139–142, 193

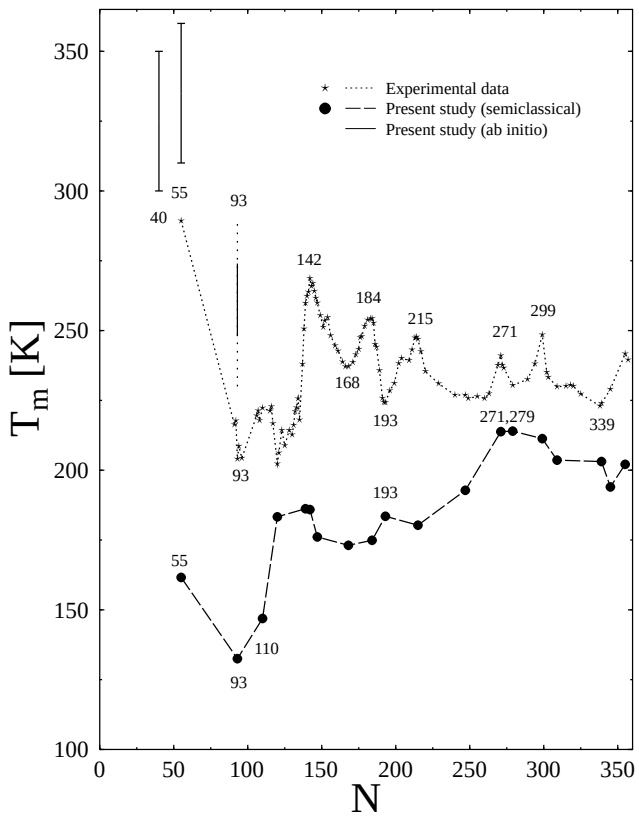

Figure 3.5: Melting temperature of sodium clusters as a function of cluster size. Our results are marked with filled circles and the experimental results of Haberland *et al.* [71, 79, 81] are marked with stars. The lines joining the points are only to guide the eye to see how the points have been connected to each other, and they do not indicate how the melting temperature behaves between the points.

and 271–279. Geometrical shell closing numbers seem to correlate with the melting temperature behaviour for clusters with less than 150 atoms, but not for the larger clusters. Experimentally, the melting temperatures for sizes smaller than 92 atoms have not been determined systematically due to the problems caused by the broadening of the phase transition.

The experimental results show the same qualitative trend when going from 55 to 93 and near size 142, as seen in our semi-classical results Fig. 3.5. However, for larger sizes the experimental curve has more maxima, and these do not seem to correlate with our results. A reason why the simulated temperatures are smaller in general than the experimental ones is most likely because of a difference in the bulk melting temperature. The semi-classical potential Eq. (3.8) used in our simulations gives a

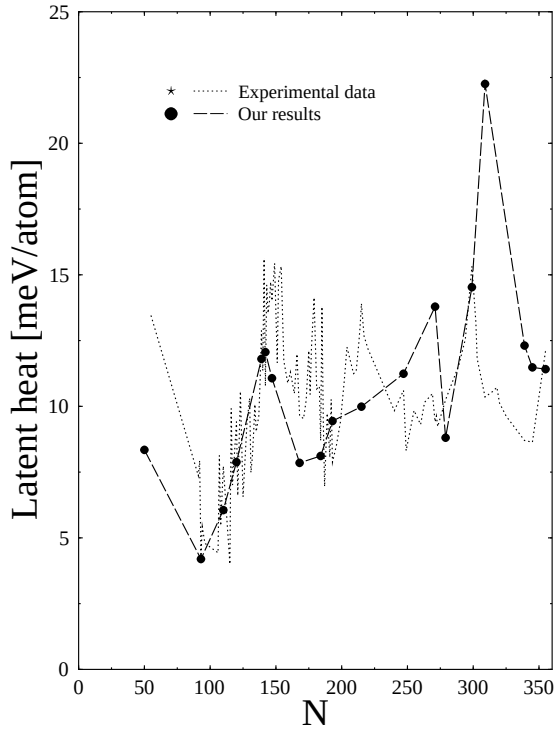

Figure 3.6: Latent heat of sodium clusters as a function of cluster size. Our results are marked with filled circles and the experimental results of Haberland *et al.* [73, 81, 99] stars. The lines joining the points are only to guide the eye to see how the points have been connected to each other, and they do not indicate how the latent heat behaves between the points.

bulk melting temperature of 333 K whereas the experimental value is 370 K.

Comparison of the experimental and our semi-classical results in Fig. 3.5 seems to indicate that by using a phenomenological potential to describe the behaviour of a simple metal one cannot reproduce the variations seen in the experimental melting temperature curve. Both curves are nonmonotonic, but the maxima and minima are not at the same places.

The latent heat of melting as a function of cluster size is shown in Fig. 3.6. The curve shows maxima at cluster sizes $N = 55$, 142, 271 and 309. The experimental latent heat of fusion for N=55–139 behaves similarly to our results [73, 81, 99], but again, the results for the larger sizes do not correlate. Comparing the latent heat of fusion (Fig. 3.6) to the melting temperature (Fig. 3.5) determined with the semi-classical method, we find that their behavior for $N = 55$–120, 139–193, and 215–271 are similar. In the size range 279–309, the peak in the latent heat curve is shifted from that of T_{melt}

towards a closed icosahedral shell. Generally, it seems that the melting temperature and the latent heat of fusion are both sensitive to the same factors. The experimental results of Schmidt *et al.* indicate that melting temperatures and latent heats of fusion could be correlated [99].

The specific heats for the solid and the liquid phases are almost constant for each phase, which is in agreement with the experimental results of Ref. [99]. The average value of the heat capacity for the solid phase is 0.275 meV/K per atom and the average value of the heat capacity for the liquid phase is 0.343 meV/K. These values are slightly higher than the experimental values of 0.245 meV/K and 0.303 meV/K for bulk solid and liquid, respectively [99], and they are comparable to the Dulong-Petit value of 0.26 meV/K.

We also studied the effect of the potential parameters p and q on the melting behavior. We chose cluster sizes of $N = 93$ and $N = 120$ and calculated the melting temperature for different values of p and q. When p is doubled and q is kept constant ($p = 20.26$, $q = 1.30$), the melting temperatures change in both cases. For Na_{93} the melting temperature increases by about 11 K, but for Na_{120} T_m decreases by about 27 K. This indicates that it is possible to change the form of the $T_m(N)$ curve by changing the parameter p. The change caused by the parameter q is smaller. When the parameter q is doubled and p is kept constant, the melting temperature of Na_{93} changes by only about 1 K and in the case of Na_{120}, the change is 8 K. Even if the form of the $T_m(N)$ curve could be changed, it should be noted that the model would not be representative of sodium.

3.10.2 Ab initio simulations

In this thesis *ab initio* calculations were made for Na^+_{59}, Na^+_{70} and Na^+_{93}. For completeness also the results of earlier *ab initio* heating simulations made at the University of Jyväskylä during the years 1996-2004 for small sodium clusters are presented here.

To obtain the energetically most favorable initial configuration for different cluster sizes, several different structures were optimized to a local minimum of the potential. The lowest energy structure (shown in Fig. 3.7) was used as a starting configuration for the simulation. The geometries of Na_8 and Na_{10} are described in Ref. [68]. The ground state configuration for Na_8 is a dodecahedron and for Na_{10} it is a bicapped antiprism. The structure of Na_{14} consists of three stacked squares with two atoms at the ends [61]. The heating simulations made for Na_{20} were started from a low energy structure suggested in Ref. [68]. The lowest energy structure of Na_{40} was obtained from an annealing simulation [69]. The initial geometry of Na^+_{55} is a perfect icosahedron as described in Ref. [68]. The low-energy structure of Na^+_{59} is an amorphous structure and was presented in Ref. [IV]. The initial configuration of Na^+_{93} was presented in Ref.

[III] and is based on an icosahedron.

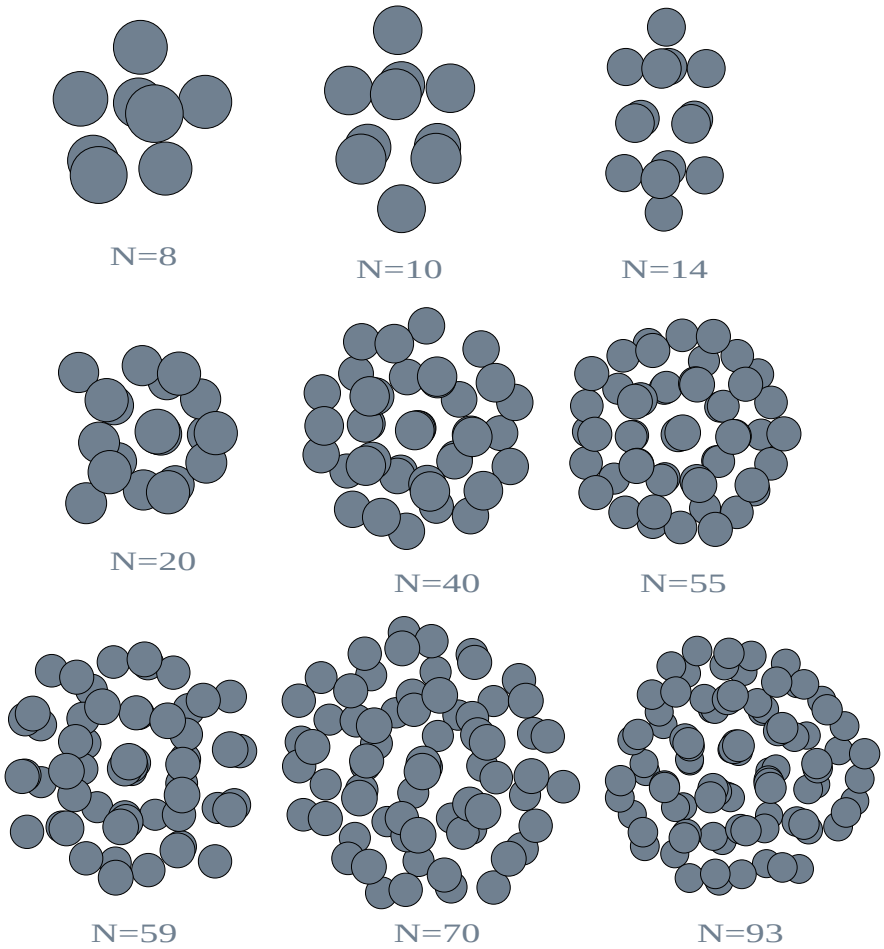

Figure 3.7: The starting geometries for *ab initio* MD simulations.

Finding the global ground state structures for small sodium clusters is an exhaustive task, and practically an impossible one if the search for minima is done only in the context of the full density functional calculation of the electronic states. In the case of Na_{59}^{+} and Na_{93}^{+} the initial configurations for the MD simulation are prepared by setting the ions to the desired geometry with a reasonable nearest neigbour distance and optimizing the structure to a local minimum on the Born-Oppenheimer potential energy surface. Even though a simulation is started from a stable structure, the system is often able to find other geometrical structures, even at energies well below the onset of diffusive motion of atoms.

The first simulations for Na_{59}^{+} were made using the close-packed BCC structure as an

Table 3.1: The nearest neighbour distance $< r_{nn} >$, the energy per atom, the vertical ionization potential vIP (the second IP of the neutral cluster), the Fermi gap Δ, and the total bandwidth of valence states W for small sodium clusters.

	$< r_{nn} >$ (Å)	E/atom (eV)	vIP (eV)	Δ (eV)	W (eV)/n
Na_{14}	2.82	5.54	-	0.40	1.81
Na_{20}	3.14	5.63	-	0.59	2.14
Na_{40}	3.35	5.70	-	0.37	2.43
Na_{55}^{+}	3.52	5.66	5.12	0.00	2.57
Na_{59}^{+}	3.46	6.18	5.44	0.45	2.99
Na_{70}^{+}	4.29	5.19	-	0.10	3.56
Na_{93}^{+}	3.98	5.72	4.84	0.19	2.57

initial configuration, because it was anticipated to be a low-energy structure. During the simulations, however, the cluster found an energetically better initial structure (This is the configuration in Fig. 3.7). This structure consists of two different shells of atoms. The core with 15 atoms has a HCP structure, but the outermost shell has both a hexagonal and a pentagonal symmetry axis. The distribution of neigbour distance, G(r), shows clear shell-like structure.

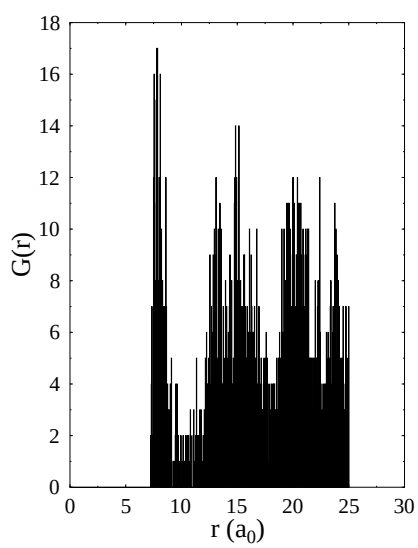

Figure 3.8: The neighbour-distance distribution $G(r)$ for Na_{70}^{+}.

In the case of 70-atom sodium clusters we used a number of initial configurations obtained by classical model potentials and presented in the Cambridge Cluster Database [141] and our net page [142]. These trial structures were then optimized to the near-

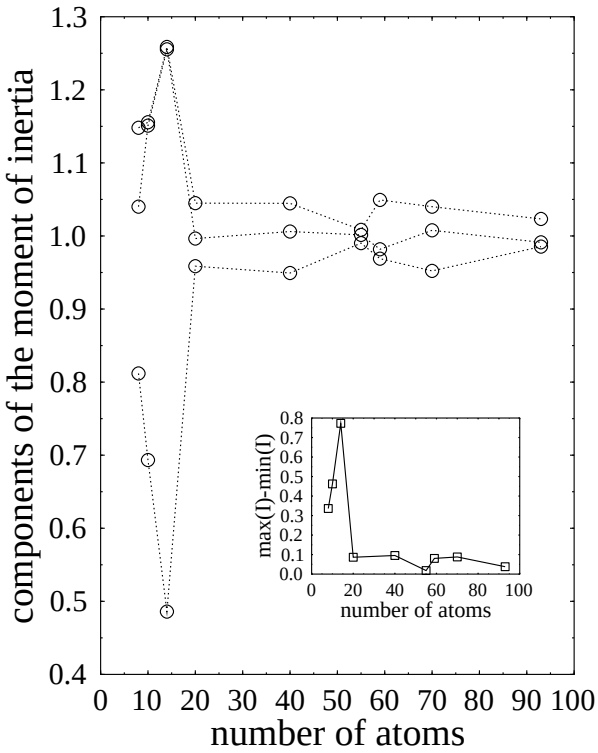

Figure 3.9: The three components of the moment of inertia (the sum of the components is normalized to 3) as a function of cluster size. The inset shows the difference between the largest and the smallest components of the moments of inertia. When the difference is zero the cluster has a cubic or spherical symmetry.

est minimum on the electronic Born-Oppenheimer energy surface. The lowest energy structure is surprisingly the lowest-energy structure of "the lead cluster" interacting via a Gupta potential [143] and this is presented in Fig. 3.7. The heating simulations were not made for Na_{70}.

The properties of the initial geometries are listed in Table 3.1. In general, the nearest neighbour distance increases with the size of the clusters. Exceptions also exist: in the case of Na^+_{59} the nearest neighbour distance is smaller than that in the case of Na^+_{55} which implies that the geometry of Na^+_{59} is (surprisingly) more close packed that the $N = 55$ icosahedron. On the other hand, the geometry of Na^+_{70} is poorly packed. The reason for this could be that the 70-atom cluster is in the middle of the two close-shell icosahedral sizes (N=55 and N=147). It is also possible that our best estimate for the geometry for Na_{70} is not the ground state geometry.

The neighbour-distance distribution, $G(r)$, for Na^+_{70} is shown in Fig. 3.8. It can be

seen that there is no clear neighbour-shell structure (cf. [IV]) and the nearest neigbour distance is clearly longer (by a_0) than in the symmetric structures (Table 3.1). It is to be noted that the nearest neigbour distance depends on how it is defined. For our calculations we defined the nearest neigbour distance to be that of two atoms separated by less than 9.5 a_0.

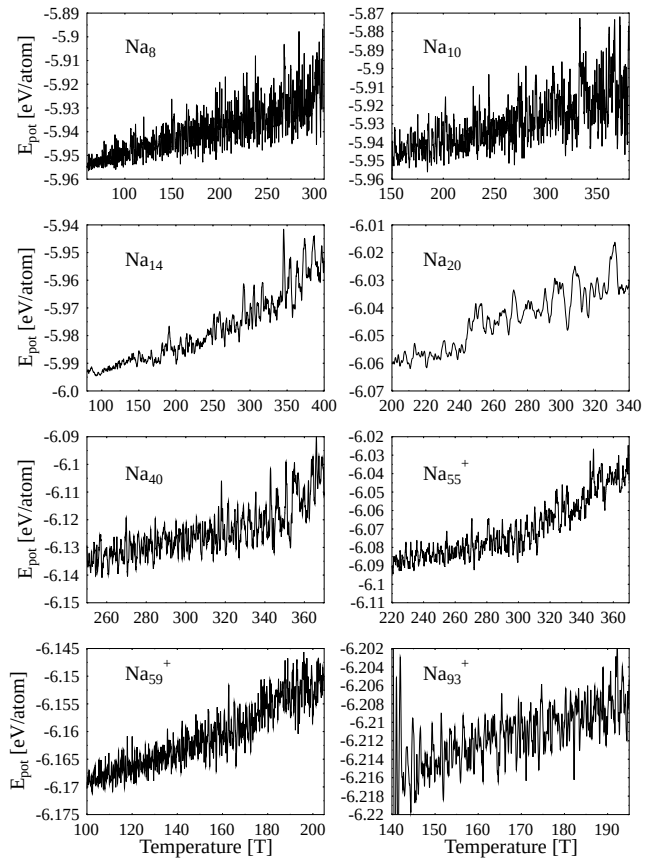

Figure 3.10: The potential energy as a function of temperature calculated using an *ab initio* MD method.

The three principal components of the moment of inertia are shown in Fig. 3.9. The components are normalized so that the sum of the components is equal to three. When the components of the moment of inertia have the same value the cluster is spherical or has a high symmetry like cubic or icosahedral. Clusters bigger than 14 atoms are relatively spherical, but for $N = 8$, 10 and 14 they are deformed. The inset of Fig. 3.9 presents the difference between the largest and the smallest components of the moments of inertia. The most spherical cluster is Na_{55}^{+} (almost a perfect icosahedron).

Na_{93}^+ is also nearly spherical. The clusters Na_8, Na_{10}, Na_{14} and Na_{70}^+ are oblate while Na_{59}^+ is prolate.

After the initial configuration is determined the clusters are equilibrated at the starting temperature for a few picoseconds before starting the heating simulations. During the heating simulation, the velocities of the ions were scaled to raise the kinetic energy of the cluster slowly. The cluster was heated linearly from the initial temperature at a heating rate of 5 or 2.5 K/ps (for Na_{14}^+ and Na_{55}^+ only the faster heating rate was used and for Na_{93} only the slower heating rate was used). These heating rates are still so high that a true thermal equilibrium is not reached during the simulations. Because the simulations use linear heating the ensemble does not correspond to a canonical or microcanonical ensemble, but for the *ab initio* method it is the only feasible way to prepare. If the simulations were done at a constant energy the calculations would require much more CPU time than would be both possible and practical.

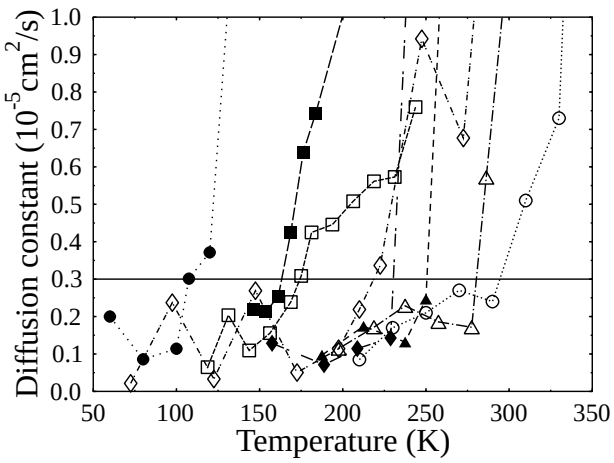

Figure 3.11: Diffusion coefficient calculated over time periods of 4 to 5 ps and plotted as a function of the average temperature in each time period. Open diamonds, triangles, circles, diamonds, open triangles, open circles, open squares, and squares represent the simulation results for Na_8, Na_{10}, Na_{14}, Na_{20}, Na_{40}, Na_{55}^+, Na_{59}^+ and Na_{93}^+, respectively.

The potential energy as a function of temperature is called the caloric curve. A large number of simulations should be done for the accurate measurements of the caloric curve and the melting temperature. Of course, this is impossible due to the limited capabilities of present day computers. In a single simulation the transition may happen anywhere in the melting region. The potential energies as a function of temperature are presented for each cluster size in Fig. 3.10. These results do not show clear melting transitions for Na_8, Na_{10}, Na_{14}, and Na_{93}^+, but for Na_{20} it can be seen that the melting starts at around 235 K, for Na_{40} at around 300 K, for Na_{55}^+ at around 310 K and for Na_{59}^+ at around 175 K. The latent heat of fusion can be also determined for these sizes.

The latent heats are 13 meV, 11 meV, 20 meV and 2.3 meV for Na_{20}, Na_{40}, Na_{55}^{+} and Na_{59}^{+}, respectively.

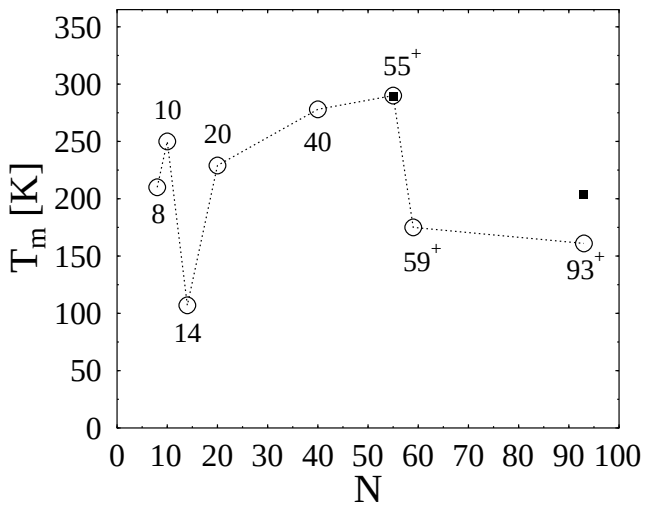

Figure 3.12: The melting temperatures as a function of cluster size. Open circles are results of *ab initio* simulations and filled squares are experimental value from Ref. [73, 81, 99].

In order to monitor the behaviour of the system in all cluster sizes, the mean square displacement of the atoms and the diffusion coefficient were determined over time intervals of 4–5 ps (corresponding to a linear rise in temperature of 10-12.5 K or 20-25 K) (Fig. 3.11). The mobility of the atoms was analyzed by determining the mean square displacement $MSD^2(t) = \sum_i |\mathbf{r}_i(t+t_0) - \mathbf{r}_i(t_0)|^2$ with respect to the atom positions at $t = t_0$. From MSD^2 the diffusion constant D can be calculated as $D = MSD^2/6s$ where s is the length of the time span used for calculating MSD^2. The melting is seen as a rapid increase of the diffusion constant. By using this approach one needs a criterion for the limiting value of D_m, the value of D when the cluster is judged to melt. We have found that D_m =0.3*10^{-5} cm^2/s agrees reasonably well with the results obtained from the caloric curve (in clusters where it could be used).

The diffusion coefficient increases with the temperature and finally reaches the value of bulk liquid sodium, which is greater than D_m =2.0*10^{-5} cm^2/s. Fig. 3.12 shows the theoretical melting temperature based on the diffusion coefficient (i.e. temperature where D exceeds D_m). It should be noted, however, that Na_{20}, Na_{40}, Na_{59}^{+} and Na_{93}^{+} are electronically magic and Na_{55}^{+} is geometrically magic. Because the melting temperature of Na_{55}^{+} is the highest, this could mean that the geometrical effect is important for melting of small sodium clusters, while the low melting temperatures of Na_{59}^{+} and Na_{93}^{+} suggests that the electronic shell structure does not stabilize the solid phase.

Our *ab initio* calculations for small sodium clusters show that Na_{55}^{+} has the highest

melting temperature. The melting temperature region deduced here for Na_{55}^{+} and Na_{93}^{+} agrees with the one determined experimentally [69, 73, 121] (see Fig. 3.12). This supports the experimentally observed tendency that sodium clusters with 55 atoms melt at temperatures higher than the other sized clusters.

To observe how the melting transition occurs, we monitored the MSD of each atom separately for the case of Na_{59}^{+}. We interpreted an individual atom to be in the 'liquid' phase when its MSD is larger than the square of the nearest neighbour distance. Fig. 3.13 shows the melting process step by step for the case of Na_{59}^{+}. The lighter color atoms are in a "liquid" phase and darker atoms are in a "solid"-like phase. There are five atoms in the liquid phase at temperature 175 K. When the temperature is increased 2 K, there are five more "liquid" atoms. If the temperature is increased a further 3 K, then 15 atoms are "liquid". At a temperature of 201 K there are 30 "liquid" atoms, i.e. the half of the atoms of the cluster is in a liquid phase. The melting seems to start from the surface, and gradually spreads to the interior of the cluster. A similar behavior was observed for Na_{93}^{+}.

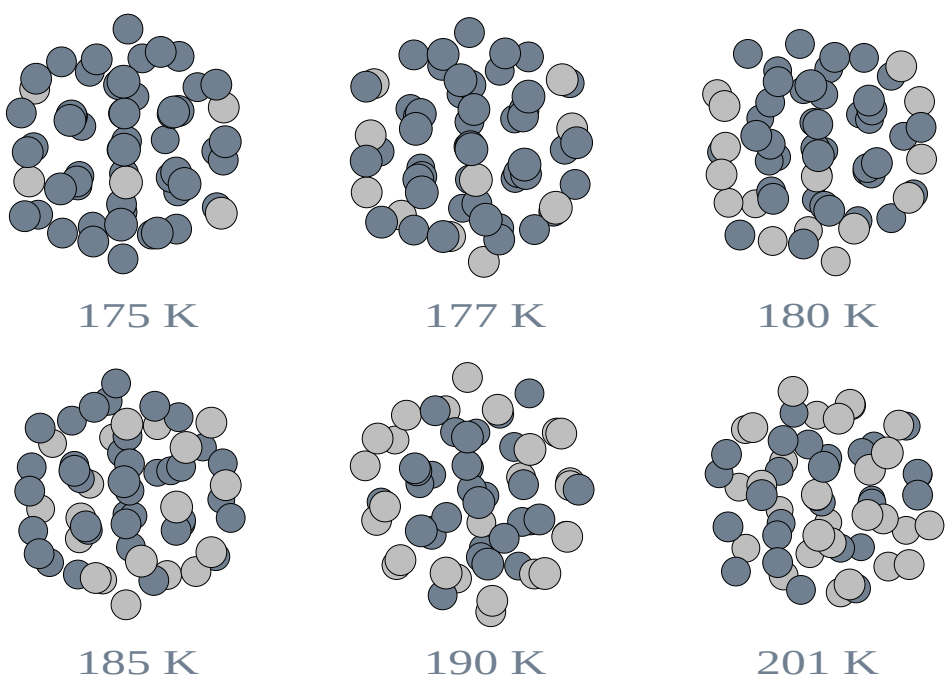

Figure 3.13: The step by step melting process for Na_{59}^{+}. The lighter color atoms are in a "liquid" phase and darker atoms are in a "solid"-like phase. Atoms which are "liquid"-like have a MSD greater than the square of the nearest neighbour distance.

4 Electronic structure

4.1 Background

The geometry of a cluster has an influence on its electronic shell structure. On the other hand, the cluster properties depend on its electronic structure. The electronic shell structure is based on the assumption that the valence electrons of a metal are almost free and move in a nearly constant potential. This is the basic idea of the jellium model. The electron numbers corresponding to full shells are called magic numbers in full analogy with nuclear physics where these numbers correspond to the numbers of neutrons and protons for which the nuclei are particularly stable. If an atom is added to a magic cluster, the new valence electron (or electrons) occupies a state with considerably higher energy. This will reduce the stability of the cluster and can be seen in the mass spectrum in the reduced abundance of the intensity [119].

The electronic structure of the jellium model can be understood by studying the solution of the radial Schrödinger equation

$$[-\frac{d^2}{dr^2} + \frac{l(l+1)}{r^2} + V(r)]P_{nl}(r) = E_{nl}P_{nl}(r), \tag{4.1}$$

where l is the angular momentum quantum number and $V(r)$ is the spherically symmetric potential. The eigenstates of this Schrödinger equation group together in subshells which are characterized by a pair of quantum numbers n and l. In an infinitely deep spherical potential well the subshells are arranged according to angular momentum: the lowest states are in the order 1s, 1p, 1d, 2s, 1f, 2p, corresponding to 2, 8, 18, 20, 34, 40 electrons [144]. Fig. 4.1 shows the level structure in details. The cluster is exceptionally stable when a group of subshells is completely filled and there is a large gap between them and the next unoccupied subshells.

The large degeneracy corresponding to large angular-momentum values $2(2l+1)$ is only possible with spherical symmetry [145]. In the case of real clusters, the shell energies split due to the reduced symmetry of the cluster. If the cluster is cubic (for example FCC, BCC) in real clusters the d shells split in to two levels having degeneracies of two and three. Similarly the f shells split (in our case we only consider the first f shell) in to three levels with degeneracies of 1, 3, and 3. When the geometry of the cluster becomes less and less symmetric, as is often the case, the shells split progressively more and finally, only the spin-degeneracy remains.

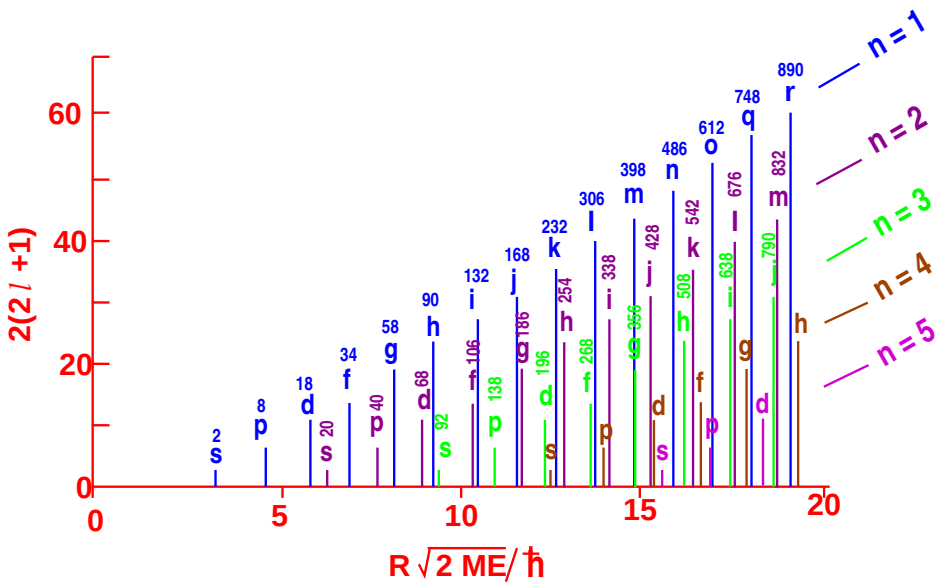

Figure 4.1: The degeneracy of states of the infinitely deep spherical well on a momentum scale [146].

In the case of real sodium clusters the shells are usually split, but the splitting is so small that large energy gaps remain between shells. Therefore for real spherical cluster it is possible to determine the shell structure. However, the overall geometry can still have influence on the electronic structure. For example, if the cluster is spherical, the energy gap at $N_e = 34$ is bigger than the gap at $N_e = 40$. If the cluster is octupole deformed like Na_{40}, its energy gap at $N_e = 40$ is bigger than for $N_e = 34$ [69]. On the other hand, the icosahedral structure is more symmetric than the FCC-structure, consequently, the d-shell in icosahedral structure remains degenerate.

In general, metallic clusters with a large energy gap between the lowest unoccupied (LUMO) and highest occupied (HOMO) level are especially stable. Spherical clusters with closed electronic shells provide the basic examples of these [147, 148]. It should be noted, however, that the Jahn-Teller deformation also opens up a clear energy gap in many nonmagic clusters (see [130] for a review).

4.2 Jellium model

The *ab initio* calculations of the electronic structure of atomic clusters are computationally intensive even for a few atoms [149] due to the large number of degrees of freedom in the system. The jellium model is used to simplify the structure and the physical properties of clusters. The discovery of the electronic magic numbers by Knight *et al.* [13] lead Ekardt [147] to use the jellium model to explain the shell structure.

The jellium model replaces the ions with a uniform positive background and ignores the discrete ionic structure. The valence electrons are then confined by this positively charged background [130]. The jellium model can be used for metals, where the valence electrons are strongly delocalized (free-electron-like). The valence electron that has an s-wave character with respect to the ionic cores does not have any directionality to the binding and so it satisfies this condition the best. This also explains why the jellium model gives such good results for the group Ia metals, particularly sodium, potassium and also to some extent for the Ib metals such as copper and silver.

In the case of sodium, the jellium model is applicable because the conduction band of sodium clusters is approximately free-electron-like, the Fermi surface is nearly spherical [119], and also because the conduction electron density is close to the equilibrium density of a homogenous electron gas [150]. For open-shell clusters the Jahn-Teller effect causes distortions from the spherical shape to minimize the total energy of the cluster and therefore the spherical jellium model cannot be used. The agreement with experiments can be improved by allowing the cluster to deform into an ellipsoidal shape [63].

4.3 Experimental observations

The first reported experiment on electronic shell structure was published in 1984 by Knight *et al.* [13]. Electronic shell structure can be demonstrated experimentally by measuring the ionization energy as a function of cluster size. Another way to observe the electronic shell structure is the use of photoelectron spectroscopy. The mass spectra of clusters also reflect the stability of cluster ion fragments. Issendorff *et al.* have made the most comprehensive experiment of size selected, negatively [151] and positively [152] charged sodium clusters by using photoelectron spectroscopy with 31 to 500 atoms. They observed the electronic shell structure directly and it was in agreement with jellium model predictions.

4.4 Results

The energy levels calculated with our *ab initio* method are shown in Fig. 4.2 for different cluster sizes. All clusters have clear energy gaps at $N_e = 2$, 8, 18, 20, 34, 58 electrons. Na_{59}^+ has only a small energy gap between 1f and 1g shells but bigger energy gap inside the 1g shell so that there is an energy gap at $N_e = 42$ instead of $N_e = 40$. These curious energy levels of Na_{59}^+ are caused by a small deformation of the structure. It is important to note that in many cluster sizes the energy gap at $N_e = 34$ is larger than at $N_e = 40$, which is expected for spherical clusters.

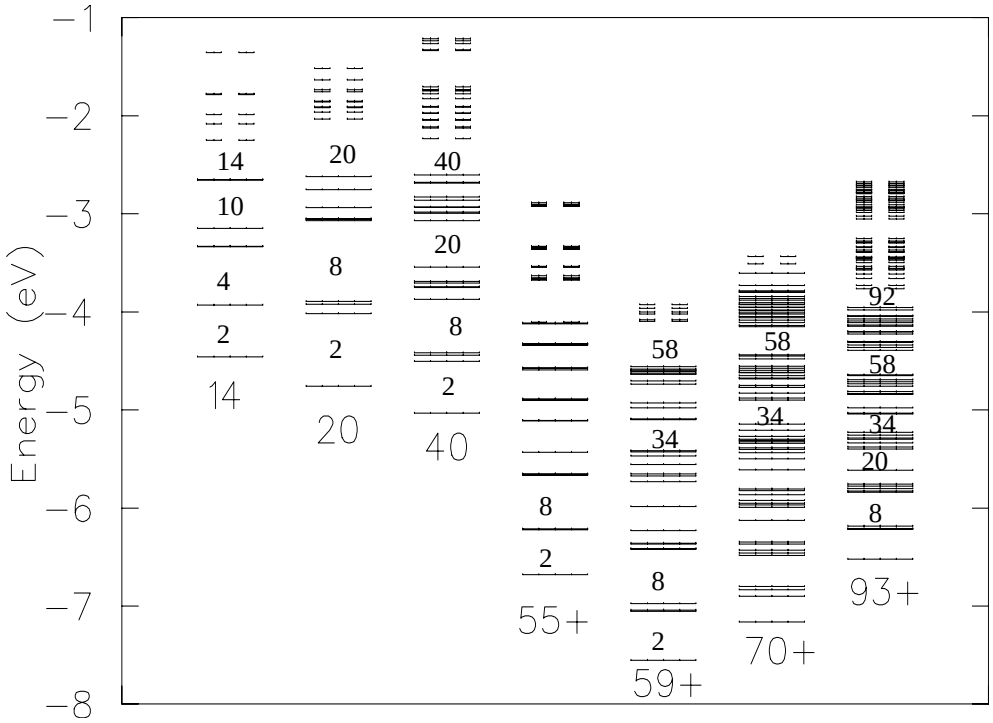

Figure 4.2: The single particle energy levels of small sodium clusters. The broken lines denote unoccupied states and long lines occupied states. The number of ions in the respective clusters are labelled below their respective levels, where the positive sign designates a cation.

From the results presented in Figure 4.2 the HOMO-LUMO gap (the energy difference between highest occupied state and lowest unoccupied state) and the width of the shells can also be calculated. These values are given in Table 3.1 together with the average nearest neighbour distance, total energy per atom and vertical ionization energy. The HOMO-LUMO gap is large in the case of Na_{20}, Na_{40} and Na_{59}^+ but relatively small in the case of Na_{93}^+. The most probable reason is that our Na_{93} results do not give the true ground state geometry, which is expected to have a much larger HOMO-LUMO gap. Na_{55}^+ and Na_{70}^+ have small HOMO-LUMO gaps, since these clus-

ters are not magic. The energy per atom (see Table 3.1) is biggest for Na_{59}^{+}, which indicates that Na_{59}^{+} is very stable.

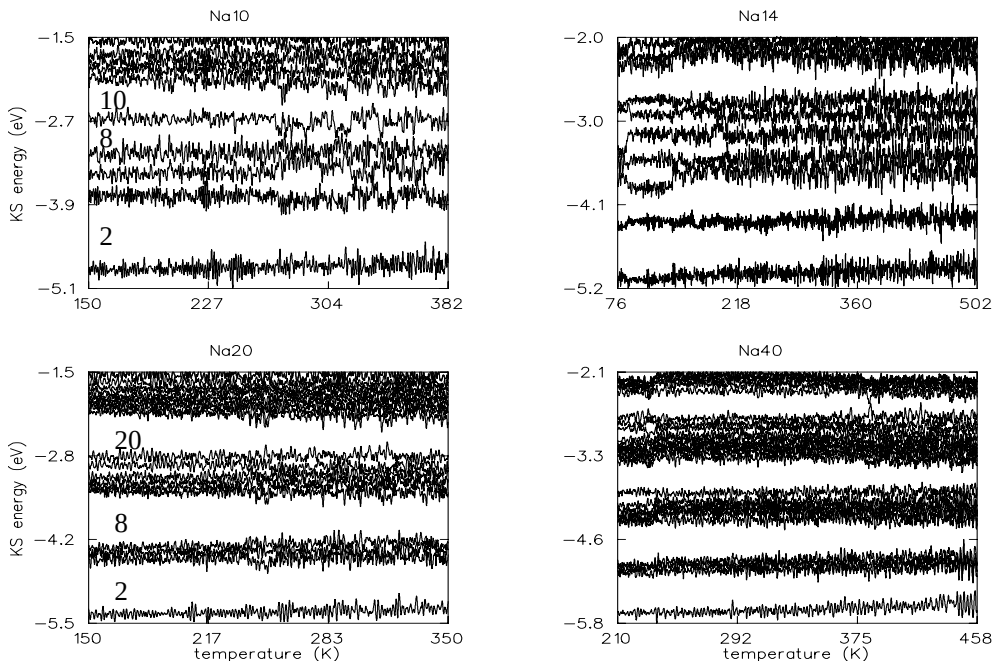

Figure 4.3: The Kohn-Sham single-electron energy eigenvalues of Na_{10}, Na_{14}, Na_{20} and Na_{40} as a function of temperature. The N_e values are indicated for clarity, but only in the diagram for Na_{10} and Na_{20}.

The dynamical simulations of sodium clusters allow us to monitor the evolution of the single-particle Kohn-Sham states as a function of temperature. The results are presented in Figs. 4.3 and 4.4. The cluster size $N = 10$ is not a magic size. As a small cluster it has a relatively large HOMO-LUMO gap as seen in Fig. 4.3 and Table 3.1. The Kohn-Sham single-electron energy eigenvalues of Na_{14} are interesting. The energy gap at $N_e = 2$ is clear, but the gap at $N_e = 8$ is not clear any more. Instead there is clear HOMO-LUMO gap at $N_e = 14$ caused by strong deformation. Also the Na_{20} undergoes a small deformation which causes a small gap at $N_e = 16$. The Kohn-Sham energy states clearly change after the cluster melts. The energy gap at $N_e = 16$ disappears and an energy gap at $N_e = 18$ opens in which is agreement with a spherical shape. The large HOMO-LUMO gap stays open during the whole simulation. This is evidence that this cluster size is electronically magic in both the liquid and solid phases.

$N = 40$ is also an electronically magic cluster size. This cluster size agrees well with the jellium model and there are large energy gaps at $N_e = 8$, 20 and 40 and smaller gaps at $N_e = 18$ and $N_e = 34$. These gaps close above ~ 350 K. The cluster size 40

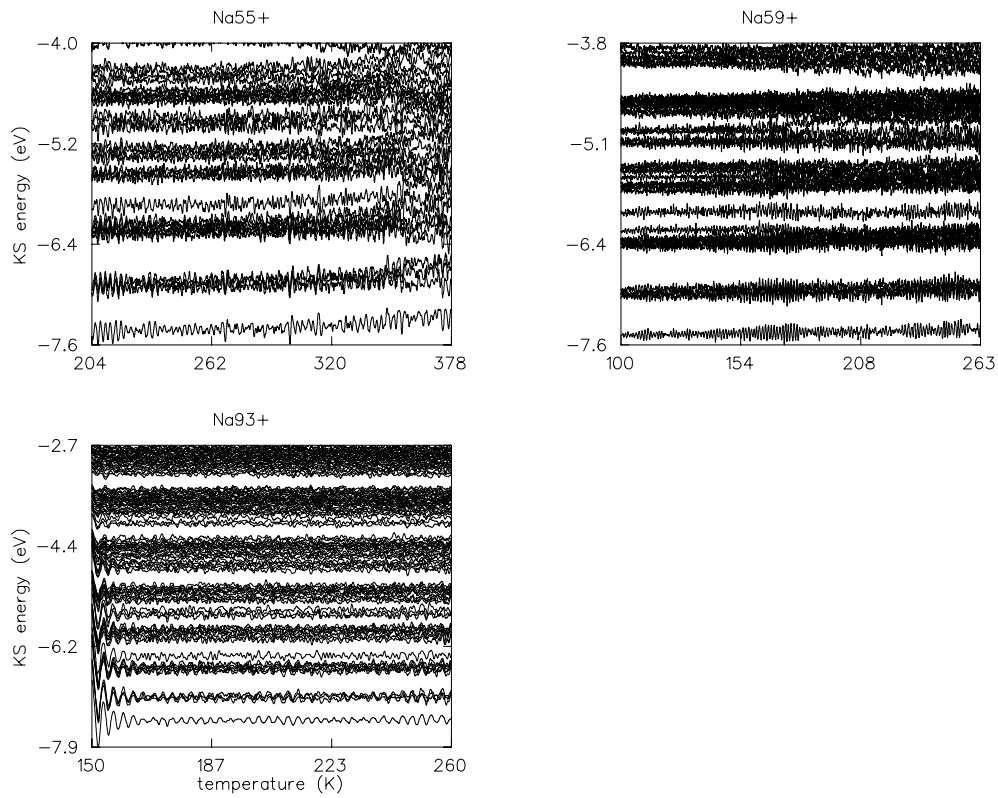

Figure 4.4: The Kohn-Sham single-electron energy eigenvalues of Na_{55}^+, Na_{59}^+ and Na_{93}^+ as a function of temperature.

shows octupole deformation [69] and therefore there is no clear energy gap at $N_e = 34$. Na_{55}^+ is a nonmagic cluster size, but it has energy gaps at $N_e = 2$, 8, 18, 20, 34 and 40. The melting transition is not seen in the evolution of Kohn-Sham states and when the temperature rises above 350 K the states fluctuate so heavily that energy gaps are no longer visible.

In the course of a heating simulation of Na_{59}^+ clusters the small energy gaps inside the 1f and 1g shells are closed and the energy gap at $N_e = 42$ electrons is changed to an energy gap at $N_e = 40$ electrons. This is consistent with the jellium model predictions [119]. This change happens when the cluster melts. However, all energy gaps, including the HOMO-LUMO gap at $N_e = 58$ remain open during the simulation which show that the liquid cluster stays electronically magic although the individual single-electron energy levels oscillate quite strongly with time. The electronic structure of Na_{93}^+ is consistent with the jellium model and all predicted energy gaps ($N_e = 2$, 8, 18, 20, 34, 40, 58, 92) can be observed. All energy gaps stay open during the simulation which is an evidence of that this cluster size is magic.

Figure 4.5 shows the density of Kohn-Sham states as a function of energy for Na_{55}^+

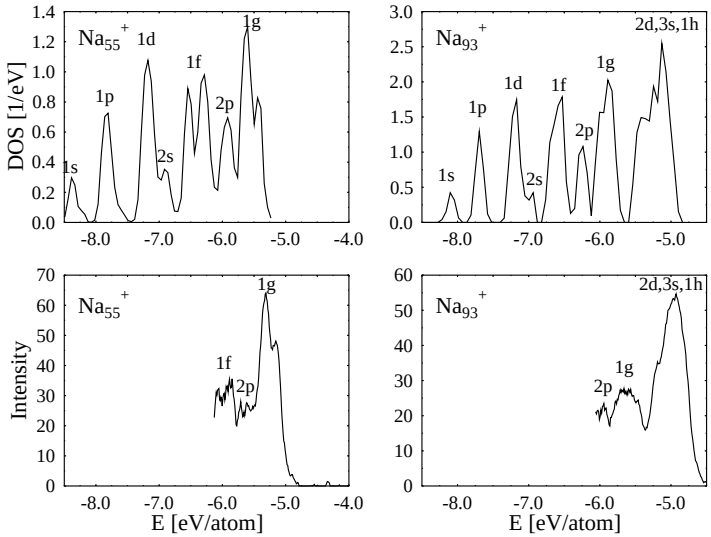

Figure 4.5: The density of Kohn-Sham single-electron states as a function of energy for Na_{55}^+ (left) and Na_{93}^+ (right) and the corresponding experimental photoelectron spectra [152].

and Na_{93}^+ with corresponding experimental results [152]. The temperature is 340 K for Na_{55}^+ and 161 K for Na_{93}^+. The electronic structures exhibit large energy gaps at $N_e = 8$, 20, 40, and 58 and smaller gaps at $N_e = 18$ and $N_e = 34$ consistent with the spherical jellium model [41, 83]. From the diagrams it can be seen that the calculated spectra are shifted from the experimental data and therefore the maximum points of the highest energy shells are somewhat lower in energy than the experimental values. This shift comes from a slight overestimation of the second ionization potential of the sodium clusters by the density functional theory. Apart from this shift, the agreement in the shape of the electron density of states of Na_{55}^+ and Na_{93}^+ with the experimental data is very good.

For the case of Na_{59}^+ the 1g shell is filled and therefore there is a pronounced energy gap between the filled shells and the empty shells. The Na_{59}^+ calculations give a theoretical energy gap between the 1g and 2p shells that is in excellent agreement with the experimental value. Simulated results clearly show the 1f shell. Experimentally, the 1f shell is only seen as a small peak in the spectrum and so only part of it appears to have been observed.

The evolution of the Kohn-Sham electron states of Na_{59}^+ (Fig. 4.6) shows that notable changes in the shell structure occur upon melting: the splitting of the 1d shell disappears around the melting temperature, the splitting of the 1f shell is removed and a gap at $N_e = 42$ electrons is closed with a new gap at $N = 40$ electrons opening. These changes are also reflected in the peak profiles of the time-averaged electron density of states at low (110 K) and high (260 K) temperatures (Fig. 4.6). The electronic density

of states spectrum at 260 K (Fig. 4.6b) correlates very well with the experimentally measured photoelectron spectrum [152] (Fig. 4.6c), apart from the shift of 0.2 eV in the position of the first peak. The numerical values for the intershell gaps from the simulation and experiment are similar. From the simulation we have (1g-2p): 0.37 eV and (2p-1f): 0.53 eV whereas for the experiment we estimate (1g-2p): 0.34 eV and (2p-1f): 0.40 eV. The good agreement of the simulated and measured gaps and the width of the 1g peak indicates that in the experiment the temperature of the Na_{59}^{+} cluster beam was around 260 K or slightly lower. From the 110 K theoretical spectrum (Fig. 4.6 a) we can predict that if the experiment (Ref. [152]) were repeated for cooler sodium clusters (around 100-150 K) and with a photon energy of about 7 eV one would be able to see the rearrangement of the 2p and 1g shells, opening of a gap at 42 electrons and splitting of the 1f shell. That would also confirm that the cluster structures found in this study are true global ground states of the Na_{59}^{+} cluster.

4.4.1 Electronic structure calculations of Al_{100} isomers

In section 2, it was mentioned that the structure of a close-packed cluster with $N = 100$ is quite interesting, as it is a very stable SFS structure based on a truncated FCC tetrahedron with stacking faults at each of the four surfaces. Another interesting fact for this size comes from the experimental photoelectron spectroscopy (PES) of Al_{100} reported by Wang *et al.* [153]. Accordingly, it was found that Al_{100} has a large energy gap between the highest and lower lying occupied orbitals.

The aim of the work presented in Ref. [II] was to reproduce experimental results [153] using the Car-Parrinello *ab initio* method and to study the applicability of our classical energy expression to actual clusters (where the true electronic structure is present). In addition to SFS structures, other low energy structures for $N = 100$ are selected from the isomers obtained from an earlier study (Chapter 1). The corresponding icosahedral and decahedral isomers were obtained from the Cambridge Cluster Database [141]: the most stable icosahedral configuration (ICO) and the Mark's decahedron for 101 atoms with one atom removed (DECA).

For a cluster with 100 aluminum atoms we use a density functional (DF) method to relax the atomic positions of the low energy isomers obtained with the simple model. The results for total energies, bond lengths, deformation, and HOMO-LUMO gaps (E_g) of Kohn-Sham orbitals are presented in Table V (Ref. [II], page 235412). The total energy differences are very small (assuming that the coordination number of the cluster is close to the maximum), and the electronic structure becomes important. According to *ab initio* simulations, the FCC isomers have the lowest energy, followed by other close-packed structures. The DECA and ICO isomers have a significantly higher energy due to the internal strain within these geometries. This is in an agree-

ment with a previous study of Al clusters [51] which showed that Al tends to form FCC geometries at a relatively early stage ($N \geq 55$).

The experimental PES of Al_N ($N = 100$–112) cluster anions [153] shows a marked gap at the threshold region. Based on our earlier experience with Al clusters [51, 154], we have compared the density of states (DOS) of close-packed Al_{100} isomers with the experimental PES. As indicated by the sizable HOMO-LUMO gaps of neutral clusters, qualitatively correct features can be observed in the DOS of lowest energy isomers. Even if we can not reproduce the exact experimental PES, we can show that we can obtain different geometries which are meaningful. CP clusters with stacking faults are potential candidates for the most stable isomer in some cases, and we have demonstrated this for Al_{100}, where the energetic difference between the FCC and SF clusters is negligible.

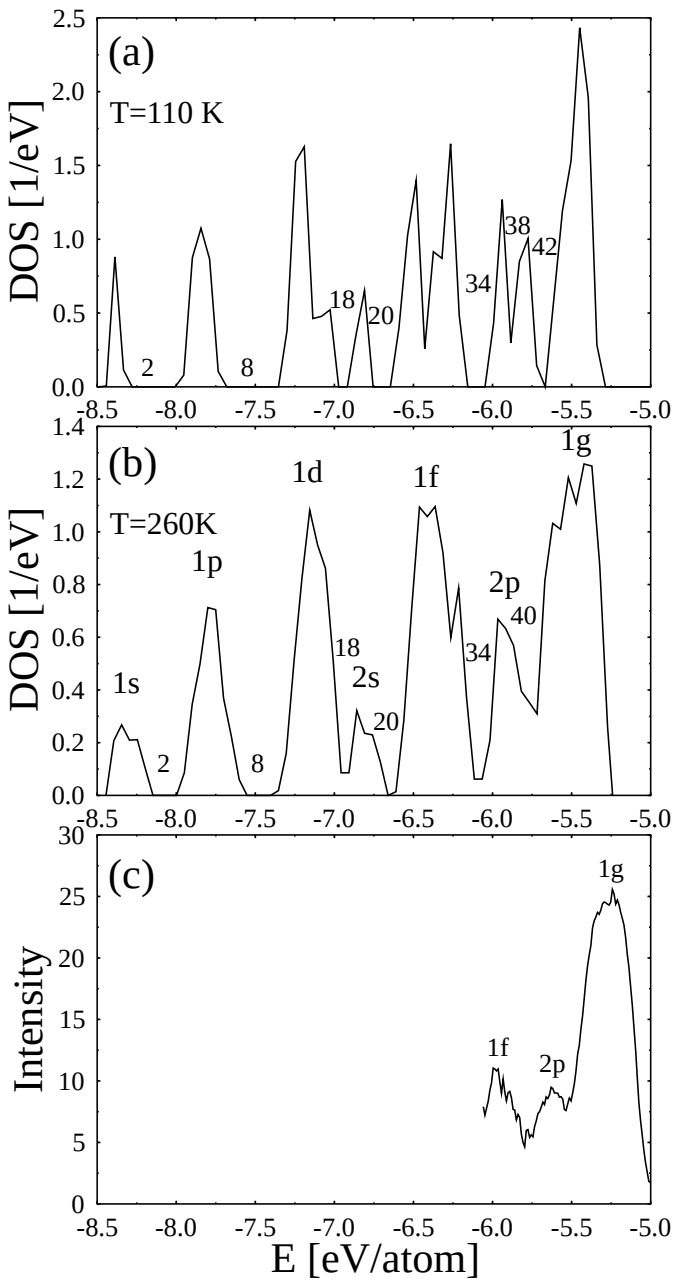

Figure 4.6: Density of Kohn-Sham states for (a) solid and (b) melted clusters at 110 K and 260 K, respectively, and (c) the experimental photoelectron spectrum of Na_{59}^{+} [152]. The shell-closing electron numbers are also shown.

5 Summary

The motivation behind the first part of this work was to study the occurrence of stacking faults and HCP structures in the ground state geometries. The structures of close-packed clusters with N = 1-110 hard spheres were studied using two types of contact interaction. Monte Carlo method and Metropolis algorithm were used to maximize the coordination number. We found 20 clusters where the structure with one or more stacking faults had a higher coordination number than any FCC structure. In most cluster sizes there are several different structures with the same coordination number. In those cases the tight binding potential which has a square root dependence on the coordination number can separate these isomers and give additional 19 sizes with stacking faults.

The ground state energy as a function of the cluster size shows that clusters with N = 12, 26, 38, 50, 59, 61, 68, 75, 79, 86, 100, and 102 have the most pronounced energy minima. These are the magic number of close-packed clusters. Of these magic sizes only the 38, 75, 79, 86, and 102 atom clusters have an FCC structure. The moments of inertia correlate well with the energy curve, showing that most of the magic clusters have also a compact geometry with a high symmetry. However, there exist structures where the energy of deformation is compensated by the large (111) facets.

Clusters with stacking faults are potential candidates for stable isomers of real clusters and this has been demonstrated for Al_{100}. The density-functional calculations show that the strain-free close-packed structures have a lower total energy than the corresponding icosahedral and decahedral isomers. The total energy differences of close-packed isomers are very small and the electronic structure becomes important. Al_{100} was chosen as a test case because of the interesting close-packed geometry found for this size and due to the exceptional shape of the photoemission spectrum [153]. However, none of the close-packed (or other studied geometries) were able to reproduce the measured spectrum.

In the second part the melting transition of sodium clusters was studied using semi-classical and *ab initio* molecular dynamics. The semi-classical molecular dynamics simulations with a tight-binding potential show that the melting temperature of small sodium clusters is a non-monotonous function of cluster size. For cluster sizes of 55, 93 and 147, the size dependence is qualitatively similar to that observed experimentally. However, for larger clusters, the simulated size-dependence of the melting temper-

ature does not follow the experimental results. From these results it seems obvious that the non-monotonic variation of the melting temperature can not be explained using semi-classical simulations, but that an *ab initio* or corresponding treatment is needed to reproduce the experimental results. The electronic structure seems to play an important role in the non-monotonic variation of the melting temperature.

Ab initio finite-temperature simulations of sodium clusters are performed using the Born-Oppenheimer local-density-approximations method. An *ab initio* molecular dynamics method was used to simulate the melting of Na_{59}^{+} and Na_{93}^{+}. The results show that Na_{59}^{+} melts around 290 K and Na_{93}^{+} around 160 K in fair agreement with the experimental result of 290 K and 204 K, respectively. The latent heat of fusion related to the melting of Na_{59}^{+} is only 2.3 meV/atom, but in the case of Na_{93}^{+} it was too small to be determined.

The *ab initio* simulations for small sodium clusters showed that even in the liquid state the clusters stay electronically magic. The HOMO-LUMO gaps stay open even though the individual single-electron energy levels oscillate quite strongly with time. The electronic structures of almost all liquid and solid sodium clusters are consistent with jellium model predictions.

The electron density of states of Na_{55}^{+} [70], Na_{59}^{+} and Na_{93}^{+} have been compared with the experimental photoelectron spectra and the agreement is excellent. Both experimental and simulated results have peaks corresponding to the electronic shells in almost the same energies.

Further work in this area requires experimental results for small potassium clusters - an interesting cluster element. If the melting temperature of small potassium clusters has similar non-monotonous size-dependence as small sodium clusters, it would not depend on the details of the pseudopotential of the group Ia metal and give possibility for a "simple" general explanation for non-monotonic behavior of the melting temperatures.

References

[I] K. Manninen, and M. Manninen, Eur. Phys. J. D **20**, 243 (2002).

[II] K. Manninen, J. Akola, and M. Manninen, Phys. Rev. B **68**, 235412 (2003).

[III] K. Manninen, A. Rytkönen, and M. Manninen, Eur. Phys. J. D. **29**,39 (2004).

[IV] K. Manninen, H. Häkkinen, and M. Manninen, Phys. Rev. A. (accepted for publication).

[V] K. Manninen, H. Häkkinen, and M. Manninen, Submitted for publications Computational Material Science.

[1] J. Akola and M. Manninen, Phys. Rev. B **63**, 193410 (2001).

[2] G. Tikhonov, V. Kasperovich, K. Wong, and V.V. Kresin, Phys. Rev. A **64**, 063202 (2001).

[3] R. Gutierrez, F. Grossmann, O. Knospe, and R. Schmidt, Phys. Rev. A **64**, 013202 (2001).

[4] S. Kümmel, J. Akola and M. Manninen, Phys. Rev. Lett. **84**, 3827 (2000).

[5] R.S. Berry, J. Chem. Faraday Trans., **86**, 2343 (1990).

[6] M.R. Hoare, Advan. Chem. Phys. **40**, 49 (1979).

[7] A.L. Mackay, Acta Cryst. **15**, 916 (1962).

[8] J.A. Northby, J. Chem. Phys. **87**, 6166 (1987).

[9] I.A. Harris, R.S. Kidwell, and J.A. Northby, Phys. Rev. Lett. **53**, 2390 (1984).

[10] J. Farges, M.F. de Feraudy, B. Raoult and G. Torchet, J. Chem. Phys. **84**, 3491 (1986).

[11] J.W. Lee and G.D. Stein, J. Phys. Chem. **91**, 2450 (1987).

[12] O. Echt, K. Sattler, and E. Recknagel, Phys. Rev. Lett, **47**, 1121 (1981).

[13] W.D. Knight, K. Clemenger, W.A. de Heer, W.A. Saunders, M.Y. Chou, and M.L. Cohen, Phys. Rev. Lett. **52**, 2141 (1984).

[14] T.P. Martin, T. Bergmann, H. Göhlich, and T. Lange, Chem. Phys. Lett. **172**, 209 (1990).

[15] T.D. Klots, B.J. Winter, E.K. Parks, and S.J. Riley, J. Chem. Phys. **92**, 2110 (1990).

[16] M. Pellarin, B. Baguenard, J.L. Viale, J. Lerme, M. Broyer, J. Miller, and A. Perez, Chem. Phys. Lett. **217**, 349 (1994).

[17] D. Rayane, P. Melinon, B. Cabaud, A. Horeau, B. Tribollet, and M. Broyer, Phys. Rev. A **39**, 6056 (1989).

[18] T.P. Martin, T. Bergmann, H. Göhlich, and T. Lange, Chem. Phys. Lett. **176**, 343 (1991).

[19] T. P. Martin, U. Näher, T. Bergmann, H. Göhlich, and T. Lange, Chem. Phys. Lett. **183**, 119 (1991).

[20] O. Echt, O. Kandler, T. Leisner, W. Miehle, and E. Recknagel, J. Chem. Soc., Faraday Trans. **86**, 2411 (1990).

[21] J.P.K. Doye and D.J. Wales, Chem. Phys. Lett. **247**, 339 (1995).

[22] J. Pillardy, and L. Piela, J. Phys. Chem. **99**, 11805 (1995).

[23] J.P.K. Doye, M.A. Miller, and D.J. Wales, J. Chem. Phys. **110**, 6896 (1998).

[24] A. Pinto, A.R. Pennisi, G. Faraci, G. D'Agostino, S. Mobilo, and F. Boscherini, Phys. Rev. B **51**, 5315 (1995).

[25] G. Schmid, Chem. Rev. **92**, 1709 (1992).

[26] T.P. Martin, U. Näher, H. Schaber, and U. Zimmermann, J.Chem. Phys. **100**, 2322 (1993).

[27] T.P. Martin, Phys. Rep. **273**, 199 (1996).

[28] A.D. Bruce, A.N. Jackson, G.J. Ackland, and N.B. Wilding, Phys. Rev. E **61**, 906 (2000).

[29] C.L. Cleveland, and U. Landman, J. Chem. Phys. **94**, 7376 (1991).

[30] W. Eckardt, Phys. Rev. B **29**, 1558 (1984).

[31] D. Reinhard, B.D. Hall, D. Ugarte, and R. Monot, Phys. Rev. B. **55**, 7868 (1997).

[32] J.P.K. Doye, Phys. Rev. B. **68**, 195418 (2003).

[33] J.P.K. Doye, and D. Wales, Phys. Rev. Lett. **86**, 5719 (2001).

[34] J.P.K. Doye, D.J. Wales, W. Branz, and F. Calvo, Phys. Rev. B **64**, 235409 (2001).

[35] J.P.K. Doye, and D.J. Wales, Phys. Rev. Lett. **86**, 5719 (2001).

[36] I.A. Harris, K.A. Norman, R.V. Mulkern, and J. A. Northby, Chem. Phys. Lett. **130**, 316 (1986).

[37] W. Branz, N. Malinowski, H. Schaber, and T.P. Martin, Chem. Phys. Lett. **328**, 245 (2000).

[38] J.P.K. Doye, D.J. Wales, S.I. Simdyankin, Faraday Discussion **118**, 159 (2001).

[39] P.M. Morse, Phys. Rev. **34**, 57 (1929).

[40] J.P.K. Doye, R.H. Leary, M. Locatelli, and F. Schoen, INFORMS J. comput., accepted.

[41] U. Röthlisberger, and W. Andreoni, J. Chem. Phys. **94**, 8129 (1991).

[42] V. Kumar, and R. Car, Phys. Rev. B **44**, 8243 (1991).

[43] J. Akola, H. Häkkinen, and M. Manninen, Phys. Rev. B **58**, 3601 (1998).

[44] J.P.K. Doye, D.J. Wales, and R.S. Berry, J. Chem. Phys. **103**, 4234 (1995).

[45] D.M. Deaven, N. Tit, J.R. Morris, and K.M. Ho, Chem. Phys. Lett. **256**, 195 (1996).

[46] J.P.K. Doye, M.A. Miller, and D.J. Wales, J. Chem. Phys. **111**, 8417 (1999).

[47] R. Leary, and J.P.K. Doye, Phys. Rev. E **60**, 6320 (1999).

[48] F. Baletto, C. Mottet, and R. Ferrando, Phys. Rev. Lett. **84**, 5544 (2000).

[49] F. Baletto, J.P.K. Doye, and R. Ferrando, Phys. Rev. Lett. **88**, 75503 (2002).

[50] J. Akola, K. Rytkönen, and M. Manninen, Eur. Phys. J. D. **16**, 21 (2001).

[51] J. Akola, M. Manninen, H. Häkkinen, U. Landman, Xi Li, and L. Wang, Phys. Rev. B **62**, 13216 (2000).

[52] A. Aguado, F. López-Gejo, and J. López, J. Phys. Chem. **110**, 4788 (1999).

[53] T.P. Martin, U. Näher, and H. Schaber, Chem. Phys. Lett. **199**, 470 (1992).

[54] J.-Y. Yi, D. Oh, and J. Bernholc, Chem. Phys. Lett. **174**, 461 (1990).

[55] F. Calvo, and J.P.K. Doye, Phys. Rev. B **69**, 125414 (2004).

[56] H. Häkkinen, and M. Manninen, Phys. Rev. B **52**, 1540 (1995).

[57] R.P. Gupta, Phys. Rev. B **23**, 6265 (1981).

[58] M.W. Finnis, and J.E. Sinclair, Phil. Mag. A **50**, 45 (1984).

[59] H. Häkkinen, J. Mansikka-aho, and M. Manninen, J. Phys.: Condens. Matter **3**, 7757 (1991).

[60] Y. Wang, T.F. George, and D.M. Lindssay, J. Chem. Phys. **86**, 3493 (1987).

[61] A. Yoshida, T. Døssing, and M. Manninen, J. Chem. Phys. **101**, 3041 (1994).

[62] H.A. Jahn and E. Teller, Proc. R. Soc. London Ser. A **161**, 220 (1937).

[63] K. Clemenger, Phys. Rev. B **32**, 1359 (1985).

[64] The SFS structure consist of FCC basis and three to four layers in stacking fault sites (SFS) in differenct directions.

[65] C.F. Weizsäcker, Z. Phys. **96**, 431 (1935).

[66] J.P. Perdew, Y. Wang, and E. Engel, Phys. Rev. Lett. **66**, 508 (1991).

[67] M. Manninen, J. Mansikka-aho, H. Nishioka, and Y. Takahashi, Z. Phys. D **31**, 259 (1994).

[68] A. Rytkönen, and M. Manninen, J. Chem. Phys. **113**, 4647 (2000).

[69] A. Rytkönen, H. Häkkinen, and M. Manninen, Phys. Rev. Lett. **80**, 3940 (1998).

[70] A. Rytkönen, H. Häkkinen, and M. Manninen, Eur. Phys. J. D **9**, 451 (1999).

[71] M. Schmidt, R. Kusche, W. Kronmüller, B. von Issendorff, and H. Haberland, Phys. Rev. Lett. **79**, 99 (1997).

[72] F. Ercolessi, W. Andreoni, and E. Tosatti, Phys. Rev. Lett. **66**, 911 (1991).

[73] M. Schmidt, R. Kusche, B. von Issendorff, and H. Haberland, Nature **393**, 238 (1998).

[74] S.L. Lai, J.Y. Gou, V. Petrova, G. Ramanath, and L.H. Allen, Phys. Rev. Lett. **77**, 99 (1996).

[75] A.A. Shvartsburg, and M.F. Jarrold, Phys. Rev. Lett. **85**, 2530 (2000).

[76] F. Calvo, and F. Spiegelmann, Phys. Rev. Lett. **82**, 2270 (1999).

[77] T.L. Beck, J. Jellinek, and R.S. Berry, J. Chem. Phys. **87**, 545 (1986).

[78] F. Calvo, and F. Spiegelmann, J. Chem. Phys. **112**, 2888 (2000).

[79] M. Schmidt, R. Kusche, W. Kronmüller, B. von Issendorff, and H. Haberland, in The Physics and Chemistry of Clusters, Proceedings of Nobel Symposium **117** (World Scientific, Singapore, 2001), p.326

[80] D.J. Wales, and R.S. Berry, J.Chem. Phys. **92**, 4283 (1989).

[81] R. Kusche, Th. Hippler, M. Schmidt, B. von Issendorff, and H. Haberland, Eur. Phys. J. D **9**, 1 (1999).

[82] A. Rytkönen, S. Valkealahti, and M. Manninen, J. Chem. Phys. **108**, 5826 (1998).

[83] V. Bonacic-Koutecky, P. Fantucci, and J. Koutecky, Chem. Rev. **91**, 1035 (1991).

[84] J. Jellinek, and I.L. Garzon, Z. Phys. D **20**, 239 (1991).

[85] F.G. Amar, and R.S. Berry, J. Chem. Phys. **85**, 5943 (1986).

[86] S. Valkealahti, and M. Manninen, Computational Material Science **1**, 123 (1993).

[87] H.-P. Cheng, and R.S. Berry, Phys. Rev. A, **45**, 7969 (1992).

[88] F. Celestini, R.J.-M. Pellenq, P. Bordarier, and B. Rousseau, Z. Phys. D, **37**, 49 (1996).

[89] R.N. Barnett, and U. Landman, Phys. Rev. B. **44**, 3226 (1991).

[90] D.J. Wales, and R.S. Berry, Phys. Rev. Lett. **73**, 2875 (1994).

[91] R.S. Berry, J. Jellinek, and G. Natanson, Phys. Rev. A **30**, 919 (1984).

[92] R.E. Kunz, and R.S. Berry, Phys. Rev. Lett. **71**, 3987 (1993).

[93] J. Jellinek, T.L. Beck, and R.S. Berry, J. Chem. Phys. **84**, 2783 (1985).

[94] H. Matsuoka, T. Hirokawa, M. Matsui, and M. Doyma, Phys. Rev. Lett. **69**, 297 (1992).

[95] C.L. Cleveland, U. Landman, and W.D. Luedtke, J. Phys. Chem. **98**, 6272 (1994).

[96] J.D. Honeycutt, and H.C. Andersen, J. Phys. Chem. **91**, 4950 (1987).

[97] E. Blaisten-Barojas, I.L. Garzön, and M. Avalos-Borja, Phys. Rev. B **36**, 8447 (1987).

[98] Ph. Buffat, and J.-P. Borel, Phys. Rev. A, **13**, 2287 (1976).

[99] M. Schmidt, J. Donges, Th. Hippler, and H. Haberland, Phys. Rev. Lett. **90**, 103401 (2003).

[100] A. Rytkönen, and M. Manninen, Eur. Phys. J. D **23**, 351 (2003).

[101] I.J. Gilvarry, Phys. Rev. **103**, 1700 (1956).

[102] W.A. Curtis, and N.W. Ashcroff, Phys. Rev. Lett. **56**, 2775 (1986).

[103] H. Löwen, Phys. Rep. (A Review Section of Physics Letters), **237**, 249 (1994).

[104] F. Calvo, and P. Labastie, J. Phys. Chem. B **102**, 2051 (1998).

[105] J.P.K. Doye, and D.J. Wales, Phys. Rev. B **59**, 2292 (1999).

[106] J.P.K. Doye, and D.J. Wales, J. Chem. Phys. **111**, 11070 (1999).

[107] N. Ju, and A. Bulgac, Phys. Rev. B **48**, 2721 (1993).

[108] J.A. Reyes-Nava, I.L. Garzon, and K. Michaelian, Phys. Rev. B **67**, 165401 (2003).

[109] A. Aguado, J. M. López, J. Alonso, and M.J. Stott, J. Phys. Chem. B **105**, 2386 (2001).

[110] A. Aguado, L.M. Molina, J.M. López, and J.A. Alonso, Eur. Phys. J. D **15**, 221 (2001).

[111] A. Vichare, D.G. Kanhere, and S.A. Blundell, Phys. Rev. B **64**, 045408 (2001).

[112] F. Calvo, and F. Spiegelman, J. Chem. Phys. **120**, 9684 (2004).

[113] P. Blaise, and S.A. Blundell, Phys. Rev. B **63**, 235409 (2001).

[114] Y. Imry, Phys. Rev. B **21**, 2042 (1980).

[115] P. Labastie, and R.L. Whetten, Phys. Rev. Lett. **65**, 1567 (1990).

[116] C. Rey, L.J. Gallego, J. Garcia-Rodeja, J.A. Alonso, and M.P. Iniguez, Phys. Rev. B **48**, 8253 (1993).

[117] F. Spiegelmann, and R. Poteau, A. Mol. Phys. **31**, 395 (1995).

[118] J. Pedersen, S.B. Bjornholm, J. Borggreen, K. Hansen, T.P. Martin, and H.D. Rasmussen, Nature **353**, 733 (1991).

[119] W.A. de Heer, Rev. Mod. Phys. **65**, 612 (1993).

[120] W. Thirring, Z. Phys. **235**, 339 (1970).

[121] M. Schmidt, R. Kusche, T. Hippler, J. Donges, W. Kronmüller, B. von Issendorff, and H. Haberland, Phys. Rev. Lett. **86**, 1191 (2001).

[122] G. Bertsch, Science **277**, 1619 (1997).

[123] R.S. Berry, Nature **393**, 212 (1998).

[124] L. Verlet, Phys. Rev. **159**, 98 (1967).

[125] W.G. Hoover, Phys. Rev. A, **31**, 1695 (1985).

[126] M.P. Allen, and D.J. Tildesley, The Computer simulations of liquids, Clarendon Press, Oxford (1987).

[127] Y. Li, E. Blaisten-Barojas, and D.A. Papaconstantopoulos, Phys. Rev. B **57**, 15519 (1998).

[128] W. Kohn, and L.J. Sham. Phys. Rev. **140**, A1133 (1965).

[129] R.N. Barnett, and U. Landman, Phys. Rev. B **48**, 2081 (1993).

[130] M. Brack, Rev. Mod. Phys. **65**, 677 (1993).

[131] N. Troullier, and J.L. Martins, Phys. Rev. B **43**, 1993 (1991).

[132] R. Car, and M. Parrinello, Phys. Rev. Lett. **55**, 2471 (1985).

[133] H. Azzoaz, J.M. Caillol, D. Levesque, and J.J. Weis, J. Chem. Phys. **96**, 4551 (1992).

[134] G. Torre-Vega, and J.H. Frederick, J. Chem. Phys. **98**, 3103 (1993).

[135] J.J. Wlodarz, J. Chem. Phys. **100**, 7476 (1994).

[136] W. Loose, and G. Ciccotti, Phys. Rev. A. **45**, 3859 (1992).

[137] D. Laria, and G. Ciccotti, Chem. Phys. **180**, 181 (1994).

[138] H. Häkkinen, and M. Manninen, Phys. Rev. Lett. **76**, 1599 (1996).

[139] R.N. Barnett, H.-P. Cheng, H. Häkkinen, and U. Landman, J. Phys. Chem. **99**, 7731 (1995).

[140] M.C. Payne, M.P. Teter, and D.C. Allan, J. Chem. Soc. Faraday Trans. **86**, 1221 (1990).

[141] The Cambridge Cluster Database, D.J. Wales, J.P.K. Doye, A. Dullweber, M.P. Hodges, F.Y. Naumkin, F. Calvo, J. Hernández-Rojas, and T.F. Middleton, URL http://www-wales.ch.cam.ac.uk/CCD.htm.

[142] URL http://www.phys.jyu.fi/research/clusters/st/index.htm

[143] J.P.K. Doye, arXiv:cond-mat/0405234v1.

[144] The number of electrons will be denoted by N_e to distinguish it from N, the number of ions in a cluster.

[145] M. Tinkham, Group theory and quantum mechanics, McGraw-Hill Book Company, 1964.

[146] T.P. Martin in Atomic Clusters and Nanoparticles edited by C. Guet, P. Hobza, F. Spiegelman, and F. David, Springer-Verlag 2001.

[147] W. Ekardt, Phys. Rev. B **29**, 1558 (1984).

[148] A. Hintermann, and M. Manninen, Phys. Rev. B **27**, 7262 (1983).

[149] V. Bonacic-Koutecky, J. Jellinek, M. Wiechert, and P. Fantucci, J. Chem. Phys. **107**, 6321 (1997).

[150] N. W. Ashcroft, and N.D. Mermin, Solid State Physics, W.B. Saunders Company, 1976.

[151] M. Moseler, B. Huber, H. Häkkinen, U. Landman, G. Wrigge, M. Astruc Hoffmann, and B. von Issendorff, Phys. Rev. B **68**, 165413 (2003).

[152] G. Wrigge, M. A. Hoffmann, and B. von Issendorff, Phys. Rev. A **65**, 63201 (2002).

[153] X. Li, H. Wu, X.-B. Wang, and L.-S. Wang, Phys. Rev. Lett. **81**, 1909 (1998).

[154] J. Akola, M. Manninen, H. Häkkinen, U. Landman, Xi Li, and L-S. Wang, Phys. Rev. B **60**, 11297 (1999).